From dry to damp and stiff mantle lithosphere by reactive melt percolation atop the Hawaiian plume

Sylvie Demouchy, Andrea Tommasi

From dry to damp and stiff mantle lithosphere by reactive melt percolation atop the Hawaiian plume

Sylvie DEMOUCHY[1*] *& Andréa TOMMASI*[1]

[1]Geosciences Montpellier, CNRS & Université de Montpellier, Montpellier, 34095, France

Correspondence to: sylvie.demouchy@umontpellier.fr

Accepted revised version to *Earth and Planetary Science Letters*

- August 2021-

https://doi.org/10.1016/j.epsl.2021.117159

* Corresponding author

Sylvie.demouchy@umontpellier.fr

Géosciences Montpellier CC060,

Université de Montpellier,

Place Eugène Bataillon,

Montpellier, 34095 cedex 5, France

Abstract

Predicting the incorporation of hydrogen (H) in the atomic structure of upper mantle minerals is a major target in geodynamics since hydration impacts essential physico-chemical properties such as the melting temperature or viscosity. Here we quantify the hydrogen concentration in olivine and pyroxenes in nine mantle peridotites from Pali (Oahu island, Hawaii), which experienced variable degrees of reactive melt percolation leading to refertilization and olivine recrystallisation. Hydrogen concentration is quantified using Fourier transform infrared spectroscopy with unpolarized and polarized light. Despite important contamination by H_2O-bearing and CO_2-bearing melt/fluid inclusions, quantitative analysis of H in olivine was successful in all samples. Quantification of H concentration in orthopyroxene was successful in most samples, excepted the two most reacted peridotites. Olivines are very H-poor (0-5 ppm H_2O wt, on average 0.8 ppm H_2O wt) and orthopyroxenes contain very small amounts of hydrogen (4 to 44 ppm H_2O wt, on average 19.5 ppm H_2O wt). The hydrogen concentration in clinopyroxene could not be quantified due to ubiquitous water-derived species trapped at the interfaces with spinel exsolutions and in hydrous melt inclusions. Despite low concentrations, H and Al in orthopyroxene are positively correlated, but comparison with a database encompassing pyroxene from peridotites from different geological settings shows that variations in degree of melting / type of metasomatism may totally overcome the crystallographic-control of Al on H incorporation. The whole-rock hydrogen concentrations estimated based on the FTIR data (2-26 ppm H_2O wt) are among the lowest in the current database for the mantle lithosphere (average at 150 ppm H_2O wt). The hydrogen concentration in orthopyroxene is positively correlated with both the recrystallized olivine fraction and the pyroxene mode, indicating that the reactive melt percolation is responsible for the limited hydration of the Pali peridotites. However, as this metasomatism did not hydrate the olivine, it did not induce mechanical weakening of the oceanic mantle lithosphere.

Keywords: oceanic lithosphere; rheology; melt percolation; hydration; NAMs; FTIR

Highlights

- Extremely low initial concentration of H in olivine and pyroxenes in an oceanic plate
- Melt percolation induced moderate H-enrichment in orthopyroxene, but not in olivine
- Such hydration cannot weaken the oceanic mantle lithosphere
- Estimated whole-rock H concentrations are among the lowest measured in peridotites
- Despite low concentrations, H and Al contents in orthopyroxene are positively correlated

1. Introduction

The incorporation of hydrogen within the atomic structure of nominally anhydrous minerals (NAMs) impacts their physical and chemical properties. Hydrogen enhances the electrical conductivity of mantle minerals (Karato, 1990) and decreases the melting temperature of peridotites (Kushiro et al., 1968). Incorporation of hydrogen in the olivine structure and of water-derived species within grain boundaries also decreases the viscosity of olivine-rich rocks (e.g., Mackwell et al., 1985, Demouchy et al., 2012; Tielke et al., 2017), but this water-induced mechanical weakening is modest when extrapolated to hydrogen concentrations, strain rates, and temperatures relevant for the Earth's upper mantle (≤30% stress decrease, see Demouchy et al., 2012).

Partial melting and metasomatism (reactive percolation of melts or fluids) impact significantly the distribution of volatile elements such as hydrogen in the mantle (e.g., Hirth and Kohlstedt, 1996, Peslier et al., 2012; Denis et al., 2015). Hydrogen (a mere proton) is highly incompatible (Dixon et al., 2002). Furthermore, laboratory experiments have quantified the hydrogen diffusion and partition coefficients in olivine and pyroxenes. Diffusion coefficients show that hydrogen can diffuse rapidly at temperatures > 800 °C in both olivine and pyroxenes. However, due to a lower activation energy, olivine should dehydrate at a faster rate than pyroxenes at lithospheric temperatures (e.g., Fig. 6 in Demouchy and Bolfan-Casanova, 2016, see also the recent study by Xu et al., 2019). Partitioning coefficients point to a simple picture where hydrogen concentrations in NAMs should decrease with increasing partial melting degrees, but increase during interaction with very hydrous fluids or H_2O-saturated melts. However, the establishment of a database on hydrogen concentrations and distribution in exhumed peridotites, which are a precious window into the deep Earth, revealed heterogenous hydrogen abundances in most geological settings and unexpected trends. For instance, mantle-

derived peridotites transported by kimberlites from deep sections of the cratonic root (>150 km) are well-known for their high hydrogen concentrations, while peridotite xenoliths from subduction environments are not distinctively enriched in hydrogen (e.g., Demouchy and Bolfan-Casanova, 2016).

The hydrogen concentrations in peridotites from the oceanic lithosphere are still undersampled, despite recent studies of peridotites dredged in ridge settings and xenoliths (Gose et al., 2009; Schmädicke et al., 2011; Warren and Hauri, 2014; Demouchy et al., 2015; Peslier and Bizimis, 2015; Peslier et al., 2015; Li et al., 2017; Li et al., 2020; Ashley et al., 2020). The mantle xenoliths carried to the surface by the Hawaiian volcanism are of particular interest, since they sample an old oceanic lithosphere impacted by plume activity. They also sample deeper sections of the oceanic lithosphere than abyssal peridotites. Only a few specimens were studied so far (six peridotites from the Salt Lake crater and one from the Pali nephelinite vent, both collected on the Oahu island, Peslier and Bizimis, 2015; Peslier et al., 2015). Here we quantify the hydrogen concentrations in nominally anhydrous minerals in a series of nine mantle xenoliths from the Pali vent, which were subjected to variable degrees of reactive melt percolation leading to changes in the microstructure and chemical composition (Tommasi et al. 2020). We aim to constrain the hydration state of the oceanic mantle lithosphere and how it was modified by plume-related reactive melt percolation.

2. Materials and methods

2.1 Geological setting and petro-structural characteristics of the studied samples

We selected a series of nine xenoliths of peridotites from Pali, a nephelinite vent from the rejuvenated-stage Honolulu basalt series on the Oahu Island (Figure 1). This volcanism,

which has carried most mantle xenoliths in Oahu, post-dates the shield volcanism by 0.6-4 Ma (Cousens and Clague 2015; Jackson and Wright, 1970). Previous petrological studies inferred that Oahu mantle xenoliths represent a residual oceanic mantle lithosphere, which was metasomatized by plume-related melts at 50-70 km of depth (e.g., Goto and Yokoyama, 1988; Keshav et al., 2007; Sen, 1988; Sen et al., 1993; Bizimis et al., 2003). The samples studied here are part of a larger collection of Hawaii mantle xenoliths used in a comprehensive petrological, microstructural and geochemical study, which aimed at determining the effects of the Hawaii plume on the seismic properties of the Pacific plate (Tommasi et al., 2020). Below, we recall briefly the main petrological and microstructural characteristics of the studied specimens (compiled in Table 1). Photomicrographs of the analyzed thick section as well as phase and olivine intragranular misorientation maps of all studied peridotites are provided in Figure S1.

Seven studied peridotites are lherzolites and two are harzburgites (PAL1 and PAL12, Table 1). Based on the microstructural classification of Tommasi et al. (2020), four are coarse-porphyroclastic (PAL1, PAL10, PAL18, and PAL23b), four are partially-recrystallized (PAL3, PAL7, PAL24, and PAL25), and one is equigranular (PAL12). The area-weighted mean grain size of olivine decreases from 2.83 mm down to 0.65 mm with increasing amount of recrystallization. The recrystallized fractions range from 1.7 to 36.5 % of the olivine area fraction, as illustrated in Figure 2 (see also Fig. S1). The olivine Mg# (defined as the atomic ratio Mg# = 100 × (Mg/(Mg+Fe)) ranges from 88.4 to 90.0 and is roughly anti-correlated with the olivine recrystallized fraction. All studied peridotites show petrographic evidence for refertilization (secondary crystallization of pyroxenes) by reactive melt percolation, such as pyroxenes with highly irregular shapes, sinuous interphase boundaries, and common cuspate terminations as illustrated in Figure 2 (see also Fig. S1). Intensity of refertilization is in general positively correlated with the olivine recrystallized fraction (Fig. 2). The correlated changes in

microstructure, mode and mineral compositions of olivine and pyroxenes and the distinctive spoon-shaped pattern of rare Earth element (REE) in pyroxenes support that recrystallisation of the original coarse-porphyroclastic microstructure of the oceanic mantle lithosphere is associated with reactive silicated melt percolation (Tommasi et al., 2020). The recrystallized fraction in these peridotites has a peculiar spatial distribution, which is not consistent with an origin in response to solid-state deformation. It is either concentrated in vein-like domains oblique to porphyroclast elongation, like in sample PAL24 (Fig. 2c), or heterogeneously dispersed along the porphyroclast grain boundaries without materializing a foliation even in samples with high recrystallized fractions, like in sample PAL12 (Fig. 2d and S1). Based on these observations, Tommasi et al. (2020) concluded that the recrystallization was static and triggered by the melt percolation events, rather than recording focused melt transport controlled by deformation.

In the presently studied series, coarse-porphyroclastic samples PAL1, PAL10, PAL18, and PAL23b are the least affected by the reactive melt percolation and thus recrystallization (<1.7-3.1% recrystallization) and the strongly recrystallized to equigranular peridotites PAL7 and PAL12 represent the opposite end-member (>30% recrystallization; Fig. 2 and Table 1). Clinopyroxenes in all samples, except PAL10, display variable enrichment in light REE (LREE) and sometimes in mid REE (MREE). In contrast, coarse orthopyroxenes show depleted patterns with a slight enrichment in LREE, except in PAL12, where orthopyroxene is variably enriched in LREE and MREE (see Fig. 9 in Tommasi et al., 2020).

2.2. Sample preparation and Fourier transform infrared spectroscopy

Thick sections were cut in random orientations relative to the foliation or lineation of the peridotites and doubly hand-polished down to a thickness between 450 and 608 μm. The

final thickness of each sample is reported in Table S1. The hydrogen speciation was detected and subsequently quantified by Fourier transform infrared spectroscopy (FTIR) in transmission mode using a Bruker IFS66v spectrometer coupled to a Bruker HYPERION microscope equipped with a liquid nitrogen-cooled MCT detector (Mercatel alloy, HgCdTe) at the Laboratoire Charles Coulomb (University of Montpellier, France). We used mid-infrared light and a KBr/Ge beam splitter. We used square apertures (100 × 100 μm or 50 × 50 μm) or rectangular apertures (100 × 50 μm) to best match optically clean zones, free-cracks or inclusion-free area. Since the measurements were performed on a rock section, in grains with variable crystallographic orientations relative to the IR beam, we mostly used unpolarized infrared spectra, following the protocol of Denis et al. (2015) and Demouchy et al., (2018). However, to establish the importance of OH bands anisotropy in orthopyroxenes, polarized measurements were also performed using a KRS-5 polarizer (thallium-bromide-iodide) placed between the mid-IR source and the sample (Fig. S2). At least 256 scans were accumulated with a resolution of 4 cm^{-1}. Each spectrum was then baseline corrected (using the OPUS software or subsequently, if needed, using the spline function in Igor pro™). Afterward, the absorbances were normalized to 1 cm thickness to yield the absorption coefficient.

Two different types of infrared calibrations were used to calculate H concentrations: (i) the empirical frequency-dependent calibration of Paterson (1982) for unpolarized infrared data and (ii) two mineral-dependent calibrations (Bell et al., 1995 for pyroxenes; Withers et al., 2012 for olivine). These calibrations result in a detection limit of about 1 ppm wt H_2O for a 1-mm-thick olivine sample (Denis et al., 2015). The estimated error from the empirical calibration in the resulting H concentration in olivine is around 30 % (Paterson, 1982); it is lower (10-15 %) for the olivine calibration of Withers et al. (2012). The maximum linear absorbance of the non-

normalized spectrum never exceeded 0.3, in agreement with the recommendations of Withers et al. (2012) for unpolarized FTIR measurements of olivine.

The frequency-dependent calibration of Paterson (1982) is given as

$$C_{OH} = \frac{\chi i}{150\zeta} \int \frac{\mathrm{k}(\upsilon)}{3780 - \upsilon} d\upsilon$$

where the following mineral specific factors χ_i (Paterson, 1982) were used based on the chemical composition in major elements of the mineral *i* (see method of calculation in Demouchy and Bolfan-Casanova, 2016): χ_{ol} = 2663 ppm wt H_2O for $Fo_{89.2}$ (average from Table 1), χ_{Opx} = 2719 ppm wt H_2O, and χ_{Cpx} = 2723 ppm wt H_2O (details are provided in Table S2). ζ is the orientation factor, which equals 1/3 for unpolarized infrared analyses (Paterson, 1982). The absorption coefficient k(υ) is a function of the wavenumber υ. Integration of the spectrum was performed between 3620 and 2900 cm^{-1} for olivine and 3700 and 3000 cm^{-1} for pyroxenes. Multiplying the average concentrations obtained by unpolarized infrared by a factor three yields estimates comparable to the sum of concentrations obtained by polarized infrared measurements along the three main crystallographic axes (see suppl. Fig. S1 in Férot and Bolfan-Casanova, 2012). Ideally, at least 10 spectra with different orientations relative to the IR beam should be analyzed and averaged to improve accuracy of the measurements (Kovàcs et al., 2008). Here this was not possible due to numerous cracks and inclusions. Often only one clean spot per olivine/pyroxene grain could be analyzed. The absorption coefficients are reported in Table 2 and S1, allowing for re-estimation of concentrations using past or future IR mineral-dependent calibrations. It also permits the comparison with published data based on the calibration of Bell et al., 2003, which is not used in this study since it overestimates hydrogen concentrations in olivine (see Withers et al., 2012 for details).

2.3 Electron backscattered diffraction and energy dispersive spectroscopy

We identified the mineralogical nature of the submicrometric solid inclusions in olivine and pyroxenes by electron backscattered diffraction (EBSD) and energy dispersive spectroscopy (EDS) in a scanning electron microscope (CamScan X500FE CrystalProbe) at Geosciences Montpellier (France). No carbon coating was applied on the surface of the thin section.

EBSD maps with step sizes ranging from 0.2 to 0.7 μm and forward scatter electron (FSE) images with a resolution up to 5 nA were acquired on small areas within each crystal using a working distance of 25 mm, a tilt angle of 70°, an acceleration voltage of 20 V, and a beam current of 10 nA. In all cases, the following phases were proposed for EBSD detection: forsterite ($(Mg)_2SiO_4$), diopside ($CaMgSi_2O_6$), enstatite ($(Mg,Fe)SiO_3$), spinel ($MgAl_2O_3$), chromite ($(Fe,Mg)Cr_2O_4$), magnetite (Fe_2O_3), rutile (TiO_2), ilmenite ($FeTiO_3$), chlorite $(Fe,Mg,Al)_6(Si,Al)_4O_{10}(OH)_8$, and hornblende $((Ca,Na,K)_2(Mg,Fe^{2+},Fe^{3+},Al)_5[Si_6(Al,Si)_2O_{22}](OH,F)_2)$. EBSD data was acquired and treated with the AZtecSynergy software from Oxford Instruments HKL. Data treatment consisted in removing wild spikes and filling non-indexed pixels when 7 neighbors with identical orientations were present.

The recrystallized fraction of olivine (Table 1, Fig. 2 and S1) has been quantified using the MTEX toolbox v.5.2 (http://mtex.googlecode.com) as the area fraction (%) of olivine grains with both a grain size < 500 μm (defined as the diameter of a circle with the same area as the grain) and a grain orientation spread (GOS), which is the average of the misorientation angles relative to the mean orientation within each grain, < 1.5°. This analysis has been performed using the EBSD orientation maps from Tommasi et al. (2020), which cover the entire full thin-sections with step sizes between 15 and 35 μm, depending on grain size.

For EDS, the following elements were detected: O, Si, Mg, Fe, Ni, Co, Cr, Mn, Al, Ca, Na, and Ti. The data were also acquired and treated with the AZtecSynergy software from Oxford Instruments HKL.

3. Results

3.1 Inclusions in nominally anhydrous mantle minerals

Infrared spectroscopy measures were performed on thick sections (450 to 608 μm). This important thickness is an advantage to assess low concentrations of hydrogen (almost as low as 1 ppm), but it is a disadvantage if one needs to avoid intracrystalline defects, such as inclusions. Optical microscopy shows that olivine and pyroxenes in the studied peridotites contain numerous inclusions as shown in Figure 3, which impact the quality of FTIR analyses and make the acquisition of reliable IR spectrum particularly challenging. We identified three types of inclusions:

(1) Small (<20 μm) scattered pale-brown to dark-brown melt/fluid inclusions (Fig. 3a) in olivine and pyroxenes; these inclusions contain water and water-derived species, which increase locally and heterogeneously the absorption in the OH^- stretching wavenumber range, leading to overestimation of the total absorbance (absorbance overestimation due to contamination). The determination of the chemical composition of these aqueous melt/fluid inclusions is beyond the scope of this study, but we discuss later their possible genesis.

(2) Colorless or blackish inclusions with a planar distribution, typical of healed cracks in mantle-derived olivines (Fig. 3b). This type of inclusions is common in olivine and is known to be CO_2-bearing (Roedder, 1965). Here these inclusions are abundant in all three mineral phases. Based on FTIR spectra, these inclusions are dry. They may have

nevertheless an opposite effect to that of aqueous melt/fluid inclusions, as the IR beam diffracts on the healed-crack plane leading to an apparent decrease of the total absorbance of the host mineral (absorbance underestimation due to diffraction).

(3) In addition, all clinopyroxenes and many orthopyroxenes (all in the two most recrystallized samples: PAL7 and PAL12) display widespread micron-scale exsolutions, which are associated with FTIR spectra contaminated by disordered water-derived species (Fig. 3). The nature of the exsolution lamellae was determined by electron backscatter diffraction and energy dispersive spectroscopy (Fig. 3h and supplementary material Figs. S3, S4, S5). Clinopyroxene contains Cr-spinel and orthopyroxene exsolutions lamellae, which occur as lamellae or needle-like crystals on {101} and (010) crystallographic planes (Fig. 3h and Fig. S3, S4, S5). Orthopyroxenes contain Cr-spinel and clinopyroxene exsolutions on the (100) plane, especially in the center of the grains (Fig. S3). Olivine also contains Cr-spinel needles on the (100) plane (Fig. S4). In all cases, clear crystallographic relations are observed between the host and exsolved phases: (111)sp // (100)px and (111)sp // (100)ol (Fig. S5). Stochiometric Cr-spinel is known to be anhydrous; it incorporates negligible H contents in its structure (e.g., Bromiley et al., 2010). The formation of the exsolution lamellae may therefore have led to partitioning and concentration of disordered water-derived species at the host/exsolution nanoscale interface. This process may explain the contaminated FTIR spectra (Fig. S3b). The chemical compositions established by energy dispersive spectroscopy do not show significant differences between spinel, orthopyroxene, and clinopyroxene occurring as exsolution lamellae or individual grains in the peridotites (Table S3).

When analyzing olivines and orthopyroxenes (in most samples), intracrystalline defects could be avoided (see an example of clean orthopyroxene on Fig. 3c) and reliable IR absorbances were obtained for multiple grains. However, disordered water-derived species such as in inclusions of type (1) and along exsolution lamellae of type (3) were ubiquitous in clinopyroxenes in all studied samples and in orthopyroxenes in samples PAL7 and PAL12 and could not be avoided for FTIR analyses. As a consequence, quantification of the H concentrations in the clinopyroxenes in none of the samples were possible. Quantifications of H concentration in the orthopyroxenes in samples PAL7 and PAL12 were also not possible, despite the acquisition of at least five spectra in different locations for each sample (cf. Fig. S3).

3.2 Infrared spectra

Representative unpolarized spectra of olivine are shown in Figure 4 together with spectra of olivine from Hawaii peridotites and other oceanic peridotites from previous studies to assess the major spectroscopic differences. All olivine spectra from this study are characterized by quasi-total absence of hydroxyl bands. Only olivine in PAL10 displays a very weak hydroxyl band located at 3250 cm^{-1}. Even the very common hydroxyl bands at 3575 and 3525 cm^{-1} linked to titanium clinohumite-like point defects (e.g., Padròn-Navarta and Hermann, 2017) in mantle-derived olivine are not visible.

Representative unpolarized spectra of orthopyroxenes are shown in Figure 5 together with polarized and unpolarized spectra from previous studies to establish the common spectroscopic bands in mantle-derived orthopyroxenes from Pali. Absorption coefficients are very low, but typical hydroxyl absorption bands in orthopyroxene located at 3600-3575 cm^{-1}, 3520 cm^{-1}, 3409 cm^{-1}, 3313 cm^{-1} are visible. Polarized spectra illustrating the pleochroic

behavior of the band at 3600 cm^{-1} characterized by a smooth shift from 3600 to 3570 cm^{-1} are presented in Fig. S2.

Despite many attempts, clinopyroxene grains in all peridotites contain too many defects, which prevent acquisition of reliable FTIR spectra. The consequences of disordered water-derived species in intracrystalline defects in diopside spectra are illustrated in Fig. S3. In these spectra, the typical OH^- band in diopside at 3630 cm^{-1} (e.g., Demouchy et al., 2015) is still discernible, but the OH^- bands of clinopyroxene at 3540 and 3460 cm^{-1} are covered by a very broad band centered at 3400 cm^{-1}, which is typical of molecular water (Keppler and Rauch, 2000). The shoulder located near 3680-3690 cm^{-1} in these spectra can be attributed to amphibole (Skogby and Rossmann, 1991).

3.3 Hydrogen concentrations

The hydrogen concentrations calculated based on the infrared spectra using the two types of IR calibrations are reported in Table 2. The integration of almost hydrogen-free olivine spectra yields, as expected, very low concentrations, which correspond to the level of noise in the spectra (<2 ppm wt H_2O). Only the coarse-porphyroclastic peridotite PAL10, which has a clear hydroxyl band at 3250 cm^{-1} (average over 5 grains), yields a hydrogen concentration in olivine above the noise level: 5 ppm wt H_2O (Fig. 4 and Table 2). The orthopyroxene spectra also yield very low hydrogen concentrations ranging from 3.8 to 44.3 ppm wt H_2O, with an average of 18.4 ppm wt H_2O. Extremely low hydrogen concentrations in orthopyroxene (<10 ppm wt H_2O) are observed in the coarse-porphyroclastic peridotites (Fig. 5 and Table 2), except PAL18, which has a concentration of 21 ppm wt H_2O. Partially recrystallized peridotites have hydrogen concentrations in orthopyroxene within the range 13-44.3 ppm wt H_2O.

3.4 Reconstructed hydrogen whole-rock concentrations

The whole-rock hydrogen concentration may be calculated based on the mineral modes for each peridotite (Table 1) and the hydrogen concentrations in olivine and orthopyroxene, if the hydrogen concentrations in spinel and clinopyroxene can be estimated. Mantle spinels are known to contain negligible H as a point defect (Bromiley et al., 2010). The rapid diffusivity of hydrogen in pyroxenes (e.g., Demouchy and Bolfan-Casanova, 2016) ensures fast equilibration of hydrogen concentration between orthopyroxenes and clinopyroxenes. Thus, we can estimate the hydrogen concentrations in clinopyroxenes based on the hydrogen partitioning coefficient $D^{H}_{cpx/opx} \approx 2$ (cf. Table 3 in Demouchy et al., 2017 and the compilation of hydrogen concentrations in NAMs from peridotitic xenoliths by Demouchy and Bolfan-Casanova, 2016). The reconstructed whole-rock hydrogen concentrations are very low, ranging from 2 to 26 ppm wt H_2O (Table S4), with an average at 10.2 ppm wt H_2O.

4. Discussion

4.1 Damp, but stiff oceanic mantle lithosphere

In the studied Pali xenolith suit, olivine is almost H-free; measured values are barely over the detection limit except in the coarse-porphyroclastic peridotite PAL10, in which olivine has 5 ppm H_2O wt. Clinopyroxenes are too contaminated by intracrystalline defects to provide reliable hydrogen concentrations. However, orthopyroxenes provide a unique and reliable data set. Here, we considered that the slow hydrogen diffusivity at temperatures below 1100 °C in orthopyroxenes ensures their reliability regarding potential H loss during ascent toward the surface (e.g., Demouchy and Bolfan-Casanova, 2016; Xu et al., 2019).

Orthopyroxenes in Pali peridotites are characterized by extremely low hydrogen concentrations (4 to 44 ppm H_2O wt., 19.5 ppm H_2O wt. on average). The entire Pali orthopyroxene suite is amongst the driest orthopyroxenes ever measured in natural peridotites as illustrated by Figure 6 (see also the database in Demouchy and Bolfan-Casanova, 2016; their Table 2 and Fig. 14a, Warren and Hauri, 2014; Ashley et al., 2020). Indeed, hydrogen concentrations in orthopyroxenes of mantle peridotites in the current database range between 10 and 383 ppm H_2O wt., and on average 145 ppm H_2O wt.; Demouchy and Bolfan-Casanova, 2016). This important difference can not be attributed to low alumina contents alone as it is similar to that in other peridotite suites (Fig. 6).

Within the Pali suite, the driest orthopyroxenes belong to the peridotites with the lowest modal content of clinopyroxene and the least recrystallized microstructures as shown by Figure 7. A positive trend is observed between orthopyroxene hydrogen concentrations and the clinopyroxene mode or the olivine recrystallized fraction, which are both proxies for increasing interaction with a percolating reactive melt (Fig. 7). These peridotites probably represent the original oceanic lithospheric mantle, not or only weakly modified by the plume activity (Tommasi et al., 2020). The low hydrogen concentrations are consistent with high degrees of partial melting occurring at the ridge, leading to dehydration of the shallow asthenospheric mantle, which flowed away from the ridge and cooled to form the oceanic mantle lithosphere. Upon impact of the Hawaii plume and maybe also before it, reactional melt percolation through the lithospheric mantle resulted in refertilization, changes in mineral compositions, REE enrichment in both clinopyroxene and in orthopyroxenes in the most reacted peridotites (Tommasi et al., 2020). Moreover, our results indicate that this reactive melt percolation has also moderately hydrated the orthopyroxenes (Fig.7).

While it is impossible to infer the time of formation of the hydrous melt inclusions in olivine and pyroxenes (type 1, section 4.1), we observed that they are not distributed as planar array or along cracks. Thus suggesting that the percolation of the hydrous melts occurred while the Pali peridotites were still in the ductile field. This type of inclusions might therefore be associated with the refertilization which produced the recrystallization, and limited hydration of the pyroxenes. In contrast, dry and CO_2-bearing inclusions were trapped in healed cracks. This suggests a late fluid percolation, occurring while the peridotites were in the brittle field, thus at a later stage at shallower depth, and may be during the xenoliths transport toward the surface. Moreover, the presence of CO_2 would lower the water fugacity of the system (Dixon and Stolper, 1995) and thus efficiently limits potential NAMs hydration (Baptiste et al., 2015).

The last type of inclusions are mineral exsolutions (Fig. 3f-h). The formation of these exsolution lamellae is consistent with the low equilibrium temperatures recorded by these peridotites (Table 1, < 960 °C). Both results suggest shallow depths of origin for the studied xenoliths and slow cooling after the reactive melt percolation responsible for both the refertilization and the moderate hydration of the orthopyroxenes. A key observation in the present study is the ubiquitous association of water-derived species associated with the exsolution lamellae (Fig. 3 and S3). We propose that the FTIR absorbance records the segregation and entrapment of water-derived species at the lamellae/host interface during the exsolution process. This mechanism does not change whole-rock hydrogen concentrations, but it changes water speciation and distribution locally. Unfortunately, water-derived species trapped at the interfaces also imped the quantification of the original hydrogen concentration in the clinopyroxenes by FTIR (Fig. S3, S4).

In summary, the present study provides evidence for moderate hydration of pyroxenes during melt-rock interactions in the shallow (<50 km depth) lithospheric mantle by a hydrous

melt. However, the present study also shows that this type of mantle processes did not hydrate the olivines in the Pali peridotites at all, independent of the intensity of the melt-rock interaction (Fig. 3 and Table 2). By consequence, it did not change the rheology of the oceanic lithospheric mantle.

4.2 Comparison with previous data for oceanic mantle lithosphere

Salt Lake Crater (SLC) peridotites, also exhumed by the rejuvenated stage volcanism in Oahu, are systematically more hydrated than Pali ones. Olivines from SLC peridotites display hydrogen loss profiles and highly variable hydrogen concentrations, which are heterogeneous even at the sample scale, but they are not H-poor (Peslier et al. 2015). Orthopyroxenes from SLC peridotites also have significantly higher hydrogen concentrations (150 ppm H_2O wt in opx, on average) than those from Pali peridotites (<20 ppm H_2O wt in opx, on average; Figs. 5 and 6). This difference in hydrogen concentrations may be explained if the Pali xenoliths represent a shallower section of the oceanic mantle lithosphere, since shallower depths will result in lower temperature and pressure, and by consequence, lower the water fugacity in the melts interacting with the peridotites. Further evidence for a shallower provenance of the Pali peridotite xenoliths relative to SLC samples encompasses: (i) the average lower equilibrium temperatures of Pali peridotites and (ii) The REE patterns of clinopyroxenes indicating reaction with melts which crystallized garnet which are only observed in SLC peridotites (Sen et al. 1993; Bizimis et al., 2003; Tommasi et al., 2020). More effective hydration of peridotites by melt-rock interaction at higher pressures is also suggested by the even higher hydrogen concentration in orthopyroxenes within garnet-bearing peridotites from geological settings such as the Ontong Java plateau (Demouchy et al., 2015) and cratonic roots (Demouchy and Bolfan-Casanova, 2016; Peslier et al., 2010; Peslier et al., 2012) as illustrated in Fig. 6.

Hydrogen-poor orthopyroxenes, consistent with extreme dehydration by partial melting, were previously reported in oceanic peridotites from Samoa Island (18-89 ppm H_2O wt, Ashley et al., 2020) and in abyssal peridotites from Mid-Atlantic ridge (MAR) at 15°N (>15 ppm H_2O wt in opx, Schmädicke et al. 2011). However, hydrogen concentrations in orthopyroxenes from other abyssal peridotites are extremely heterogeneous and most studies report moderate to high concentrations (Fig. 6). High hydrogen concentrations are reported, for instance, for peridotites dredged from the MAR at 15°N and near the Kane (159-270 ppm H_2O wt., Gose 2009, not reported in Fig. 6 since alumina contents are not available) and the Vema transform faults (119-383 ppm H_2O wt, Li et al. 2020), as well as in the Southwest Indian ridge (SWIR; 24-262 ppm H_2O wt, Li et al. 2017; 8-378 ppm H_2O wt, Warren and Hauri, 2014) and in the East Pacific Rise (EPR) at Hess Deep (83-233 ppm H_2O wt, Hesse et al. 2015). Part of these variations might result from a high spatial variability and on average lower degrees of partial melting in slow spreading ridges, such as the MAR and SWIR, relative to the fast spreading EPR. However, the extreme variability in hydrogen concentrations, apparently independent of the orthopyroxene alumina content in peridotites dredged along the Vema transform faults, the SWIR, and the EPR (Fig. 6), may only be interpreted as due to post-melting metasomatism (e.g., Warren and Hauri, 2014; Hesse et al. 2015; Li et al. 2020). A similar trend is found for peridotite xenoliths from Ichinomegata (Fig. 6), which have sampled the Japan back-arc system (Satsukawa et al., 2017), suggesting that a different mechanism controls the hydrogen incorporation in orthopyroxene in these four cases.

Analysis of the variation in hydrogen concentration as a function of the alumina content in many individual peridotite suites illustrates the crystallographic control of Al on hydrogen incorporation in orthopyroxene previously established by Mierdel et al. (2007). However, the significant offset between the sub-parallel trends of the linear fits for the different peridotite

suites (Fig. 6) points to a non-negligible effect of the physico-chemical conditions under which the melt-rock reactions occur and impact the hydrogen concentration of pyroxenes.

The analysis of the full dataset highlights two different trends: the first one is characterized by a simple crystallographic control of Al on hydrogen incorporation in orthopyroxene (Pali, SCL, Samoa, North China Craton), whereas the second one (Vema, EPR, Ichinomegata) is characterized by noticeable H enrichment at constant Al content (low dip vs. vertical trends in Fig. 6). The data for the SWIR peridotites displays a mixture of the two trends (Fig. 6). A major petrological difference between peridotite suites displaying the first or the second trend is that the first group, to which the Pali peridotites belong, was subjected to extensive reaction with melts which changed both their microstructure and composition. Whereas the second group, which encompasses the abyssal peridotites and the Ichinomegata xenoliths, was submitted to limited (cryptic) metasomatism by evolved fluids at shallow depths. The abyssal peridotites data, in particular, imply that the latter process may effectively hydrate orthopyroxene. Hydrogen contents in olivine in abyssal peridotites could not be measured due to serpentinization, but in Ichinomegata xenolithic olivine has low hydrogen concentrations (4-16 ppm H_2O wt), suggesting that this process also does not significantly hydrate olivine.

5. Conclusion

We have identified very low hydrogen concentrations in olivine and orthopyroxene in Pali peridotites, which sample the mantle of the Pacific plate atop the Hawaii plume. Analysis of the FTIR spectra on the light of microstructural and geochemical evidence for variable degrees of reactive melt-rock interaction indicates that olivine is H-free, whereas orthopyroxene underwent moderate hydration in response to reactive percolation of melts. The present data implies that the oceanic lithospheric mantle at the intermediate depths sampled by the Pali

xenoliths was initially extremely H-poor. It also shows that reactive melt percolation can moderately hydrate the pyroxenes, but did not hydrate the co-existing olivine. Therefore, no significant impact is expected on the strength of the oceanic lithospheric mantle. This study also highlights hydroxyl-bearing interfaces associated with spinel exsolution lamellae in pyroxenes, which are ubiquitous in the most refertilized peridotites. These exsolution lamellae imply slow cooling after the melt-rock interactions, consistent with shallow (<50 km) equilibrium depths. Integration of the present data and reanalysis of the database of orthopyroxene H concentration in peridotites highlights two hydration trends, which are likely related to different types of metasomatic agents, as well as a marked effect of the pressure and temperature conditions on the hydration of orthopyroxenes by reactive melt percolation. This may explain the heterogeneity in hydrogen concentration in orthopyroxenes observed amongst Hawaiian peridotites from Pali and SLC and amongst abyssal peridotites.

Acknowledgements

The authors sincerely thank F. Barou for help with the mineral inclusion characterization by EBSD and EDS, J. Warren and E. J. Chin for constructive reviews, and H. Bureau for fruitful discussions on melt inclusions in mantle and magmatic minerals. C. Nevado and D. Delmas provided high-quality sections for FTIR, EDS, and EBSD. D. Maurin and the IR-Raman technological Platform of University of Montpellier are acknowledged for vibrational experiments. The EBSD-SEM national facility at Geoscience Montpellier is supported by the Institut National de Sciences de l'Univers (INSU) from the Centre National de la Recherche Scientifique (CNRS, France). The raw FTIR data are available upon request from the corresponding author, treated FTIR spectra are available at the Zenodo OpenAIRE repository under the doi:10.5281/zenodo/4645597. EBSD data used to generate the phase maps

and grain orientation maps presented in Fig. 2 and supplementary material S1 are available at the Zenodo OpenAIRE repository under the doi:10.5281/zenodo.3754078.

References

Ashley, A.W., Bizimis, M., Peslier, A.H., Jackson, M., 2020. Metasomatism and Hydration of the Oceanic Lithosphere: a Case Study of Peridotite Xenoliths from Samoa. J. Petrol. 61, 1–29. doi:10.1093/petrology/egaa028

Baptiste, V., Demouchy, S., Keshav, S., Parat, F., Bolfan-Casanova, N., Condamine, P., Cordier, P., 2015. Decrease of hydrogen incorporation in forsterite from CO_2-H_2O-rich kimberlitic liquid. American Mineralogist 100, 1912–1920. doi:10.2138/am-2015-5200

Bell, D.R., Ihinger, P.D., Rossman, G.R., 1995. Quantitative and analysis of trace OH in garnet and pyroxenes. Am. Mineral. 80, 465–474.

Bell, D.R., Rossman, G.R., Maldener, J., Endisch, D., Rauch, F., 2003. Hydroxide in olivine: a quantitative determination of the absolute amount and calibration of the IR spectrum. J. Geophys. Res. 108. doi: 10.1029/2001JB000679

Bizimis, M., Sen, G., Salters, V.J.M., 2003. Hf–Nd isotope decoupling in the oceanic lithosphere: constraints from spinel peridotites from Oahu, Hawaii☆. Earth and Planetary Science Letters 217, 43–58. doi:10.1016/S0012-821X(03)00598-3

Bromiley, G.D., Nestola, F., Redfern, S.A.T., Zhang, M., 2010. Water incorporation in synthetic and natural $MgAl_2O_4$ spinel. Geochim. Cosmochim. Acta 74, 705–718. doi:10.1016/j.gca.2009.10.015

Chin, E.J., Soustelle, V., Liu, Y., 2020. An SPO-induced CPO in composite mantle xenoliths correlated with increasing melt-rock interaction. Geochim. Cosmochim. Acta 278, 199-218.

Cousens, B.L., Clague, D.A., 2015. Shield to rejuvenated stage volcanism on Kauai and Niihau, Hawaiian islands. J. Petrol., 56, 1547–1584.

Demouchy, S., Bolfan-Casanova, N., 2016. Distribution and transport of hydrogen in the lithospheric mantle: A review. Lithos 240-243, 402–425. doi:10.1016/j.lithos.2015.11.012

Demouchy, S., Ishikawa, A., Tommasi, A., Alard, O., Keshav, S., 2015. Characterization of hydration in the mantle lithosphere: Peridotite xenoliths from the Ontong Java Plateau as an example. Lithos, 212-215, 189–201. doi:10.1016/j.lithos.2014.11.005

Demouchy, S., Shcheka, S., Denis, C.M.M., Thoraval, C., 2017. Subsolidus hydrogen partitioning between nominally anhydrous minerals in garnet-bearing peridotite. Am. Min. 102, 1822–1831. doi:10.2138/am-2017-6089

Demouchy, S., Tommasi, A., Barou, F., Mainprice, D., Cordier, P., 2012. Deformation of olivine in torsion under hydrous conditions. Phys. Earth Planet. Int. 202-203, 57–70. doi:10.1029/2008GL036611

Demouchy, S., Tommasi, A., Ionov, D., Higgie, K., Carlson, R.W., 2018. Microstructures, water contents, and seismic properties of the mantle lithosphere beneath the northern limit of the Hangay dome, Mongolia. Geochem. Geophys. Geosyst. 2018GC007931. doi:10.1029/2018GC007931

Denis, C.M.M., Alard, O., Demouchy, S., 2015. Water content and hydrogen behaviour during metasomatism in the uppermost mantle beneath Ray Pic volcano (Massif Central, France). Lithos, 236-237, 256–274. doi: 10.1016/j.lithos.2015.08.013

Dixon, J.E., Leist, L., Langmuir, C., Schilling J.-G., 2002. Recycled dehydrated lithosphere observed in plume-influence mid-ocean ridge – basalt. Nature, 420, 385-389.

Dixon, J.E., Stolper, E.M., 1995. An experimental study of water and carbon dioxide solubilities in mid-ocean ridge basaltic liquids. Part II: applications to degassing. J. Petrol. 36 (6), 1633–1646.

Férot, A., Bolfan-Casanova, N., 2012. Water storage capacity in olivine and pyroxene to 14 GPa: Implications for the water content of the Earth's upper mantle and nature of seismic discontinuities. Earth Planet. Sci. Lett. 349-350, 218–230.

Gose J., Schmädicke, E., Beran A., 2009. Water in enstatite from Mid-Atlantic Ridge peridotite: Evidence for the water content of suboceanic mantle? Geology. 37(6); 543-546. Doi:10.1130/G25558A.

Goto, A., Yokoyama, K. 1988. Lherzolite inclusions in olivine nephelinite tuff from Salt Lake Crater, Hawaii. Lithos, 21, 67–80.

Hesse, K.T., Gose, J., Stalder, R., Schmädicke, E., 2015. Water in orthopyroxene from abyssal spinel peridotites of the East Pacific Rise (ODP Leg 147: Hess Deep). Lithos 232, 23–34. doi: 10.1016/j.lithos.2015.06.011.

Hirth, G., Kohlstedt, D.L., 1996. Water in the oceanic upper mantle: implications for rheology, melt extraction and the evolution of the lithosphere. Earth Planet. Sci. Lett. 144, 93–108.

Jackson, E. D., Wright, T.L., 1970. Xenoliths in the Honolulu volcanic series, Hawaii. J. Petrol., 11, 405–433.

Karato, S.I., 1990. The role of hydrogen diffusivity in the electrical conductivity of the upper mantle. Nature, 347, 272–273.

Keppler, H., Rauch, M., 2000, Water solubility in nominally anhydrous minerals measured by FTIR and ^{1}H MAS NMR: Effect of sample preparation. Phys. Chem. Minerals., 27, 371-376.

Keshav, S., Sen, G., Presnall, D. C., 2007. Garnet-bearing xenoliths from Salt Lake Crater, Oahu, Hawaii: High-pressure fractional crystallization in the oceanic mantle. J. Petrol., 48, 1681–1724.

Kovàcs, I., Green, H.W., Rosenthal, A., Hermann, J., O'Neill, H.S.C., Hibberson, W.O., Udvardi, B., 2012. An experimental study of water in nominally anhydrous minerals in the upper mantle near water-saturated solidus. J. Petrol 53, 2067–2093.

Kushiro, I., Syono, Y., Akimoto, S.-I.: Melting of a peridotite nodule at high pressures and high water pressures, J. Geophys. Res., 73 (18), 6023-6029, 1968.

Li, W., Soustelle, V., Jin, Z., Li, H., Chen, T., Tao, C., 2017. Origins of water content variations in the suboceanic upper mantle: Insight from Southwest Indian Ridge abyssal peridotites. Geochem. Geophys. Geosyst. 18, 1298–1329. doi:10.1002/2016GC006767

Li, P., Xia, Q.-K., Dallai, L., Bonatti, E., Brunelli, D., Cipriani, A., Ligi, M., 2020. High H_2O Content in Pyroxenes of Residual Mantle Peridotites at a Mid Atlantic Ridge Segment. Scientific Reports, 10: 579. doi:10.1038/s41598-019-57344-4

Mackwell, S.J., Kohlstedt, D.L., Paterson, M.S., 1985. The role of water in the deformation of olivine single crystals. J. Geophys. Res. 90, 11–319–11–333.

Mierdel, K., Keppler, H., Smyth, J.R., Langerhorst, F., 2007. Water solubility in aluminous orthopyroxene and the origin of the asthenosphere. Science 315, 364–368.

Murphy, M., J., Businge, S., 2011. Orographic influence on an Oahu flood. Mon. Weather Rev., 139, 2198-2217. doi: 10.1175/2010MWR3357.1

Padròn-Navarta, J.A., Hermann, J., 2017. A Subsolidus Olivine Water Solubility Equation for the Earth's Upper Mantle. J. Geophys. Res. Solid Earth 122, 9862–9880. doi:10.1002/2017JB014510

Paterson, M.S., 1982. The determination of hydroxyl by infrared absorption in quartz, silicate glasses and similar materials. Bull. Minéral. 105, 20–29.

Peslier, A.H., Bizimis, M., 2015. Water in Hawaiian peridotite minerals: A case for a dry metasomatized oceanic mantle lithosphere. Geochem. Geophys. Geosyst. 16, 1211–1232. doi: 10.1002/2015GC005780

Peslier, A.H., Bizimis, M., Matney, M., 2015. Water disequilibrium in olivines from Hawaiian peridotites: Recent metasomatism, H diffusion and magma ascent rates. Geochim. Cosmochim. Acta, 1–66. doi: 10.1016/j.gca.2015.01.030.

Peslier, A.H., Woodland, A.B., Bell, D.R., Lazarov, M., 2010. Olivine water contents in the continental lithosphere and the longevity of cratons. Nature 467, 78–83.

Peslier, A.H., Woodland, A.B., Bell, D.R., Lazarov, M., Lapen, T.J., 2012. Metasomatic control of water contents in the kaapvaal cratonic mantle. Geochim. Cosmochim. Acta 97, 213–246.

Roedder E., 1965. Liquid CO_2 inclusions in olivine-bearing nodules and phenocrysts from basalts. Am. Min. 50. 1776-1782.

Satsukawa, T., Godard, M., Demouchy, S., Michibayashi, K., Ildefonse, B., 2017. Chemical interactions in the subduction factory: New insights from an in situ trace element and hydrogen study of the Ichinomegata and Oki-Dogo mantle xenoliths (Japan). Geochim. Cosmochim. Acta 208, 234–267. doi: 10.1016/j.gca.2017.03.042

Schmädicke, E., Gose, J., Will, T.M., 2011. Heterogeneous mantle underneath the North Atlantic: Evidence from water in orthopyroxene, mineral composition and equilibrium conditions of spinel peridotite from different locations at the Mid-Atlantic Ridge. Lithos 125, 308–320. doi: 10.1016/j.lithos.2011.02.014

Sen, G., 1988. Petrogenesis of spinel lherzolite and pyroxenite suite xenoliths from the Koolau shield, Oahu, Hawaii: Implications for petrology of the post-eruptive lithosphere beneath Oahu. Contrib. Min. Petrol., 100, 61–91.

Sen, G., Frey, F. A., Shimizu, N., Leeman, W. P., 1993. Evolution of the lithosphere beneath Oahu, Hawaii: Rare Earth element abundances in mantle xenoliths. Earth Planet. Sci. Lett., 119, 53–69. doi: 10.1016/0012-821x(93)90006-u

Skogby, H., Rossmann, G.R., 1991. The intensity of amphibole OH bands in the infrared absorption spectrum. Phys. Chem. Minerals., 18, 64-68.

Tielke, J. A., Zimmerman, M. E, Kohlstedt, D. L. 2017. Hydrolytic weakening in olivine single crystals, J. Geophys. Res. 122(5), 3465-3479, doi:10.1002/(ISSN)2169-9356

Tommasi, A., Mameri, L., Godard, M., 2020. Textural and compositional changes in the lithospheric mantle atop the Hawaiian plume: Consequences for seismic properties. Geochem. Geophys. Geosyst. 21, 19–29. doi:10.1029/2020GC009138

Warren, J.M., Hauri, E., 2014. Pyroxenes as tracers of mantle water variations. J. Geophys. Res. 119, 1851–1881. doi:10.1002/2013JB010328

Withers, A.C., Bureau, H., Raepsaet, C., Hirschmann, M.M., 2012. Calibration of infrared spectroscopy by elastic recoil detection analysis of H in synthetic olivine. Chem. Geol. 334, 92–98

Yang, X.-Z., Xia, Q.-K., Deloule, E., Dallai, L., Fan, Q.-C., Feng, M., 2008. Water in minerals of the continental lithospheric mantle and overlying lower crust: A comparative study of peridotite and granulite xenoliths from the North China Craton. Chem. Geol. 256, 33–45. doi:10.1016/j.chemgeo.2008.07.020

Xu, Y., Tang, W., Hui, H., Rudnick, R.L., Shang, S., Zhang, Z., 2019. Reconciling the discrepancy between the dehydration rates in mantle olivine and pyroxene during xenolith emplacement. Geochim. Cosmochim. Acta 267, 179-195

Figure captions

Figure 1: Maps of Hawaii archipelago and Oahu island with the location of the Pali vent (samples from this study) and the Salt Lake Crater (previous studies). Maps are redrawn from Murphy and Businger (2011).

Figure 2: Microstructure and mineralogy of Pali peridotites representative of different degrees of reactive melt interaction, recorded by increasing static recrystallization and enrichment in pyroxenes (refertilization). (a) Coarse-porphyroclastic peridotite PAL10 with ~3% of recrystallized fraction, representative of the original oceanic plate mantle. (b) Moderately recrystallized peridotite PAL3, with ~9% recrystallized fraction pervasively distributed in the sample. (c) Partially recrystallized peridotite PAL2A, in which olivine recrystallization and refertilization are concentrated in a vein-like domain that cross-cuts the original coarse-porphyroblastic microstructure. (d) Equigranular peridotite PAL12, characterized by a high recrystallized fraction (>30%) and pyroxene enrichment pervasively distributed. In the EBSD phase maps, the recrystallized olivine grains are defined as olivine grains with sizes < 500 μm and a grain orientation spread < 1.5° (see main text for details and Figure S1).

Figure 3: Photomicrographs of nominally anhydrous minerals in the studied Pali peridotites showing: (a) melt inclusions in olivine in sample PAL12; (b) closed planar cracks hosting CO_2-bearing inclusions in olivine in sample PAL1; (c) clean enstatite in sample PAL23a; (d)

exsolution lamellae in enstatite in PAL23a; (e) exsolution lamellae in diopside in PAL18; (f) exsolution lamellae in diopside in PAL10; (g) higher resolution image of exsolution lamellae in diopside in PAL7 in natural light; (h) electron forward scatter image of exsolution lamellae in diopside in PAL7, also shown in the insert is the corresponding phase map obtained by EBSD measurements (see details in Fig. S4).

Figure 4: Representative unpolarized infrared spectra for olivine from this study. For comparison, FTIR olivine spectra from previous studies are also shown (Pali and Salt Lake, Oahu island from Peslier et al., 2015 and Ontong-Java plateau, Malaïta Island from Demouchy et al., 2015). Spectra are offset vertically for clarity and are all normalized to 1 cm thickness.

Figure 5: Representative unpolarized infrared spectra for enstatite from this study. For comparison, FTIR enstatite spectra from previous studies are also shown (Pali and Salt Lake, Oahu island from Peslier et al., 2015 and Ontong-Java plateau (Malaïta Island) from Demouchy et al., 2015). Spectra are offset vertically for clarity and are all normalized to 1 cm thickness.

Figure 6: Hydrogen concentration (in ppm H_2O wt) as a function of alumina content (in wt.%) in orthopyroxene in the studied peridotites compared to data from previous studies. Hawaii (Oahu): Peslier et al., 2015; Samoa (Avai'i): Ashley et al., 2020; Ontong-Java Plateau (Malaïta): Demouchy et al., 2015; Oki-Dogo and Ichino-Megata: Satsukawa et al., 2017; North China Craton: Yang et al., 2008; Chin et al., 2020 (NB: in this study, the H concentrations were obtained by secondary ion mass spectrometry (SIMS)); Mid Atlantic Ridge (MAR) (drilling and dredging): Schmädicke et al., 2011; Li et al., 2020; Southwest Indian Ridge (SWIR): Li et al., 2017 and Warren and Hauri, 2014 (NB: in this study, the H concentrations were obtained

by SIMS). World-wide database: Demouchy and Bolfan-Casanova, 2016. Linear fits to several series are only shown to highlight trends; R^2 values range between 0.6 and 0.65: (this study R^2=0.6, Hannuoba R^2=0.6, Nushan R^2=0.6, SLC, R^2=0.65). Slopes for these trends range between 13.5 and 25.4. Error bars are lower than the symbol size for alumina contents and around 15% for hydrogen concentration.

Figure 7. (a) Hydrogen concentration in orthopyroxene (in ppm H_2O wt) as a function of the mode (%) of clinopyroxene or orthopyroxene in the studied Pali peridotites. (b) Hydrogen concentration in orthopyroxene (in ppm H_2O wt) as a function of the area fraction of recrystallized olivine in the peridotite, which is defined as olivine grains with sizes < 500 μm and a grain orientation spread < 1.5° 'see main text for details and Figure S1).

Table captions

Table 1: Summary of the key petrological and microstructural indicators of the studied Pali peridotites, from Oahu Island, Hawaii. Further data are provided in Table S5.

Table 2: Average integrated absorption coefficients and corresponding hydrogen concentrations of olivine and orthopyroxene. Result for each spectrum is given in Table S1.

Table 1. Summary of the key petrological and microstructural indicators of the selected peridotites from Oahu Island, Hawaï. Further data are provided in Table S5.

Samples	Microstructure[1]	Mineral fraction[1] %				Av. Ol[1] Mg#	Eq. T[1] ° C	Ol GS[1] μm	Opx GS[1] μm	Cpx GS[1] μm	Fract. Rex Ol[2] %
		Ol	Opx	Cpx	Sp						
PAL1	Coarse-porphyroclastic	69	29	2	<1	89.0	908	2815	2100	306	2.97
PAL3	Recrystallized	50	30	16	4	88.4	890	1707	2093	900	9.00
PAL7	Recrystallized	68	19	13	<1	89.4	851	683	1751	445	36.45
PAL10	Coarse-porphyroclastic	69	20	10	1	90.0	866	2007	59	944	3.05
PAL12	Equigranular	72	23	4	<1	88.4	953	728	1075	252	30.76
PAL18	Coarse-porphyroclastic	65	22	13	<1	89.9	874	2402	1027	1106	1.68
PAL23a	Coarse-porphyroclastic	70	21	8	1	89.7	881	1853	1506	715	2.03
PAL24	Recrystallized	52	33	13	2	88.7	958	1427	4511	696	17.39
PAL25b	Recrystallized	55	29	14	2	89.0	911	1520	1164	665	10.80

[1] Data originally reported in Tommasi et al., (2020). Av. Ol stand for the average olivine composition express as Mg# = 100 x Mg/(Mg/Fe); Eq. T stands for calculated equilibrium temperature; GS is for average mineral grain size ponderated by the area.

[2] Fract. Rex. Ol: Fraction of recrystallized olivine from EBSD data from Tommasi et al, (2020) reprocessed for this study. It equals the area fraction of olivine grains with grain size < 500 μm and having a grain orientation spread below 1.5 °, see main text for details and Figure S1 for EBSD maps.

Table 2. Average integrated absorption coefficients and corresponding hydrogen concentrations in olivine and orthopyroxene. Result for each spectrum is given in Table S1.

Sample	Microstructure	Fract. Rex Ol[1] %	Nb of spectra	Av. Abs. coeff cm^2	Av. ppm H_2O wt[2]	Av. ppm H_2O wt[3]	Nb of spectra	Av. Abs. coeff cm^2	Av. ppm H_2O wt[2]	Av. ppm H_2O wt[4]
			Olivine				*Orthopyroxene*			
PAL1	Coarse-porphyroclastic	2.97	15	4.7	1.1	1.7	6	19.2	4.3	3.8
PAL3	Recrystalized	9.00	5	2.9	<1	1.1	5	64.8	14	13
PAL7	Recrystalized	36.45	5	7.6	1.2	2.7	n.d.	n.d.	n.d.	n.d.
PAL10	Coarse-porphyroclastic	3.05	5	14.9	1.0	5.3	10	45.8	9.0	9.1
PAL12	Equigranular	30.76	5	4.7	<1	1.7	n.d.	n.d.	n.d.	n.d.
PAL18	Coarse-porphyroclastic	1.68	5	7.3	1.3	2.6	19	105.5	21.7	21.0
PAL23a	Coarse-porphyroclastic	2.03	5	4.9	1.0	1.8	5	34.7	8.0	6.9
PAL24	Recrystalized	17.39	5	5.1	1.0	1.8	13	152.1	32.5	30.6
PAL25b	Recrystalized	10.80	6	4.5	0.8	1.6	4	222.2	46.8	44.3

[1] Fract. Rex. Ol: EBSD data from Tommasi et al, (2020) reprocessed for this study (area fraction for olivine with grain size < 500 μm and a grain orientation spread < 1.5 °, see main text for details and Figure S1 for EBSD maps).
[2] Calibration of Paterson (1982) for olivine or orthopyroxene (see main text for details). Error is estimated around 30 %.
[3] Calibration of Withers et al. (2012) for olivine. Error is estimated around 15 %.
[4] Calibration of Bell et al., (1995) for orthopyroxenes. Error is estimated around 15 %.

Demouchy and Tommasi, Fig. 1

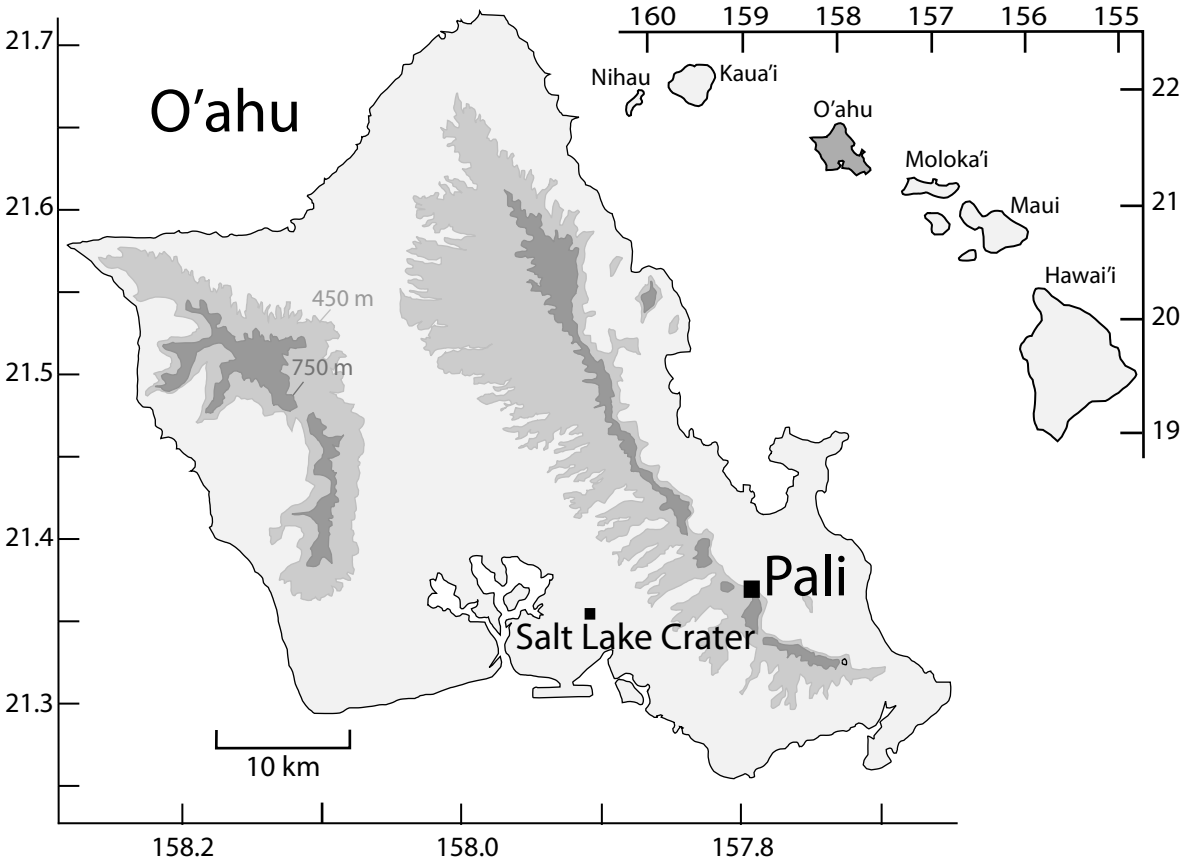

Demouchy and Tommasi, Fig. 2

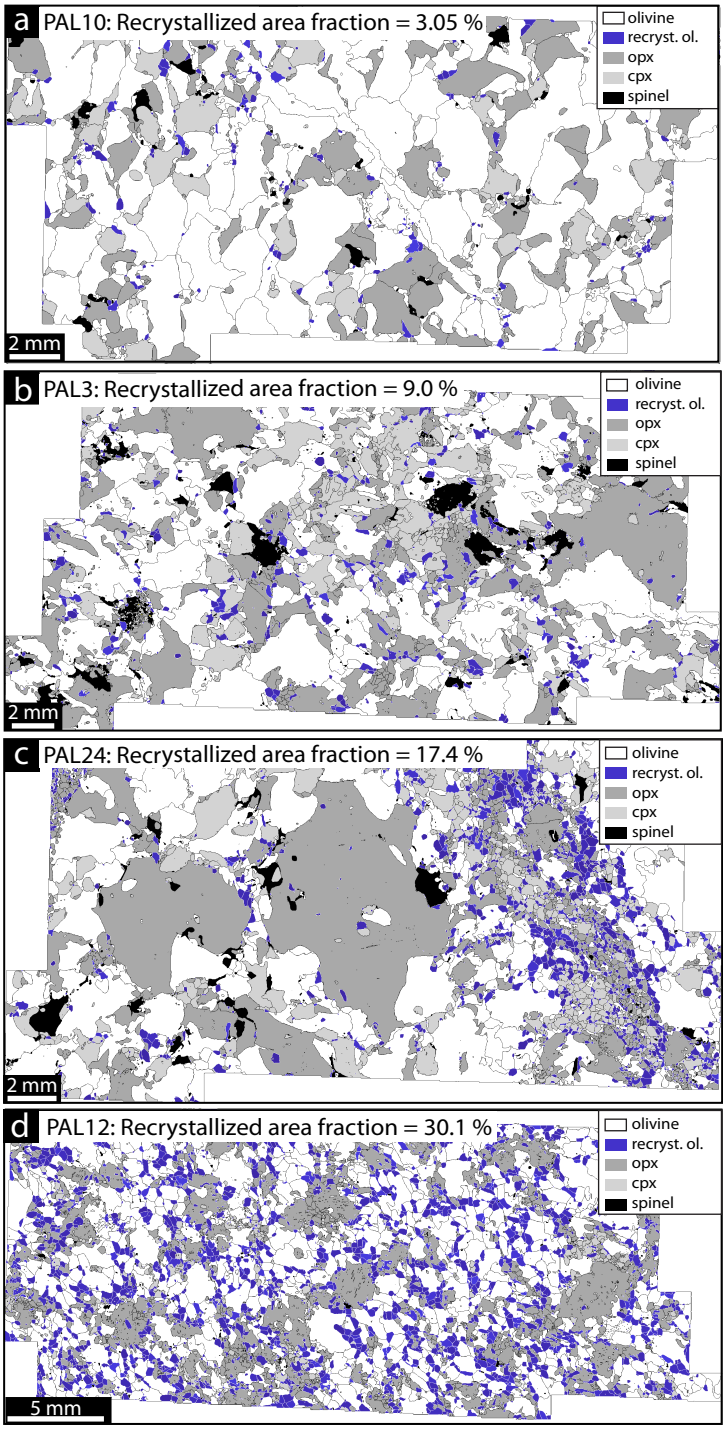

Demouchy and Tommasi, Fig. 3R

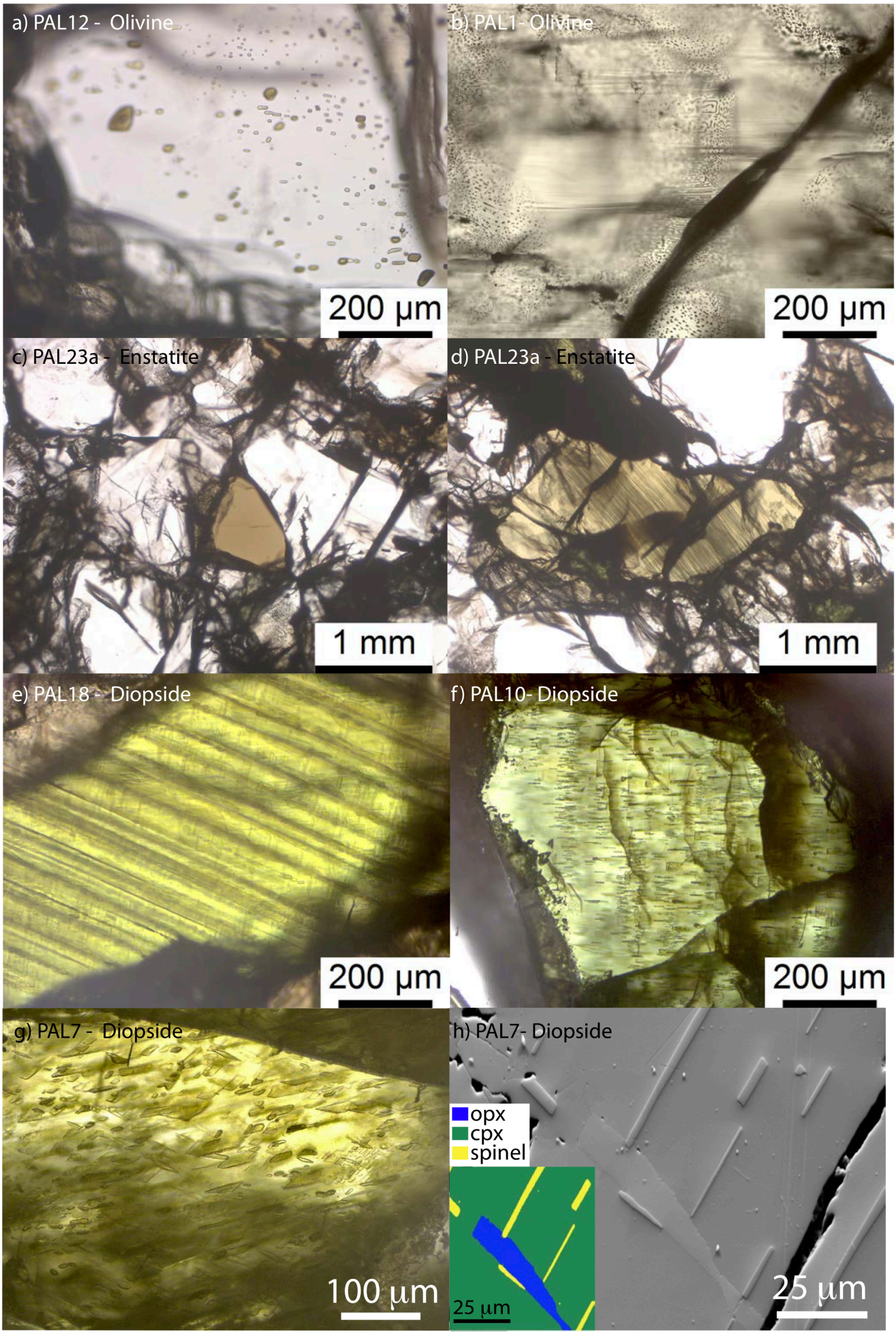

Demouchy and Tommasi, Fig. 4

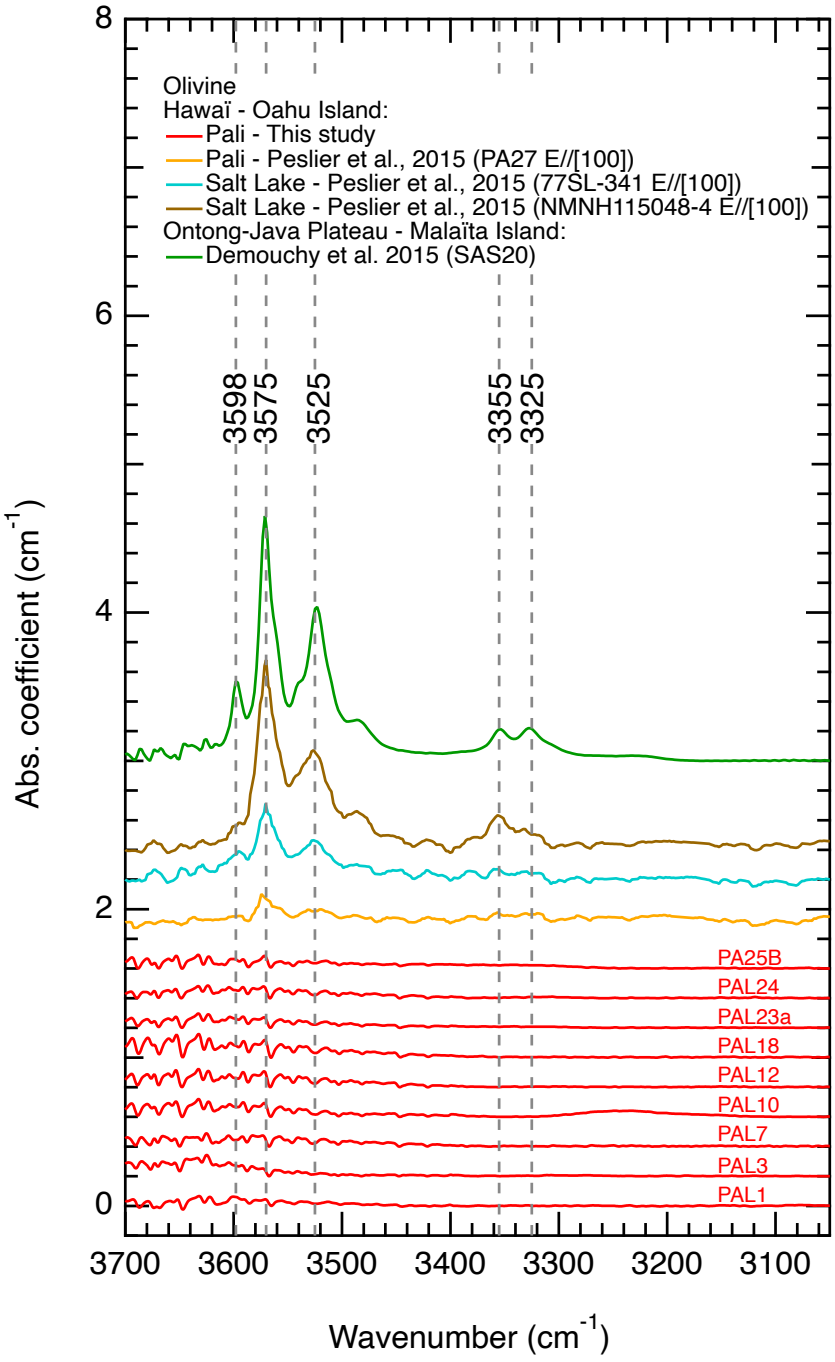

Demouchy and Tommasi, Fig. 5

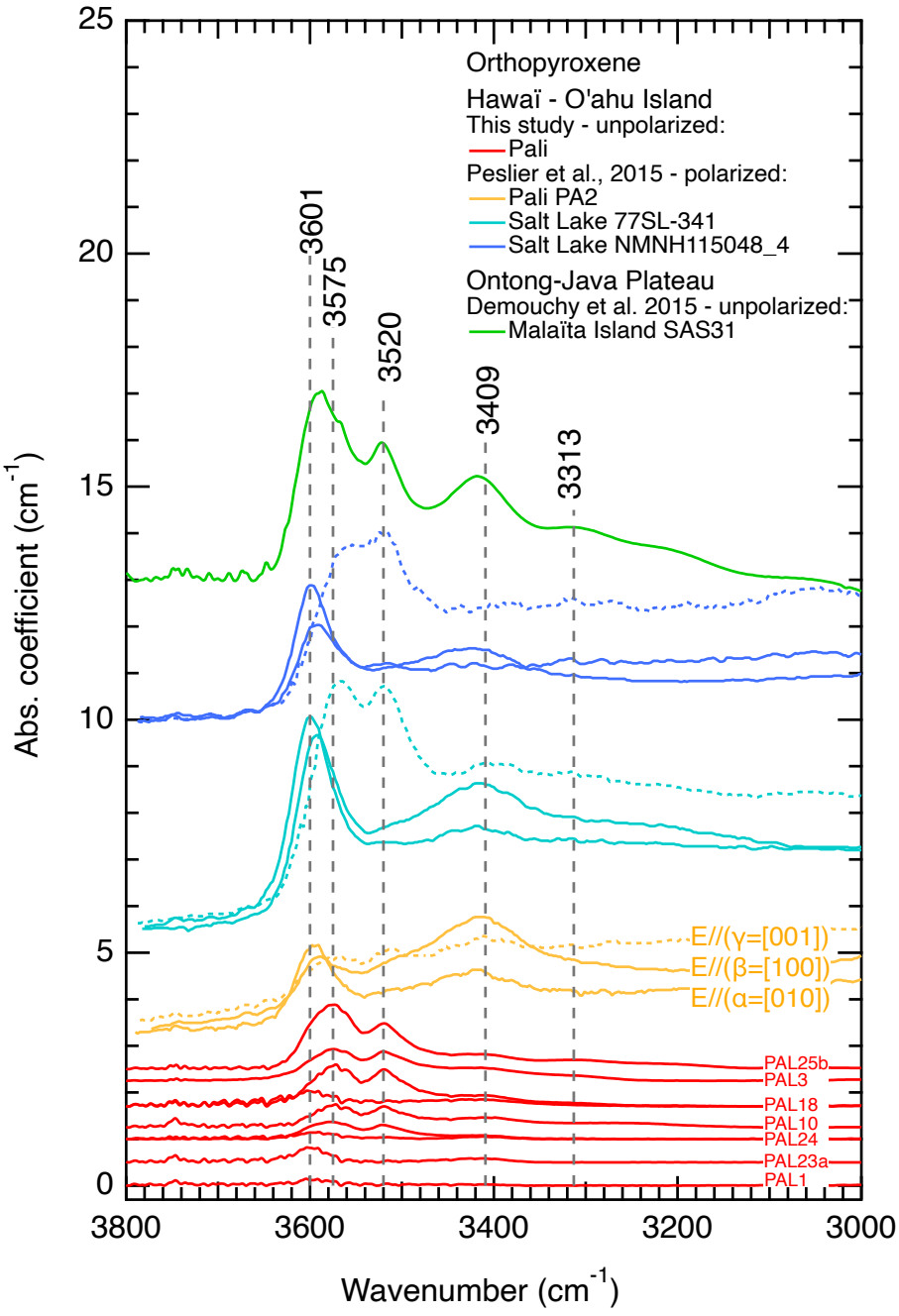

Demouchy and Tommasi, Fig. 6R

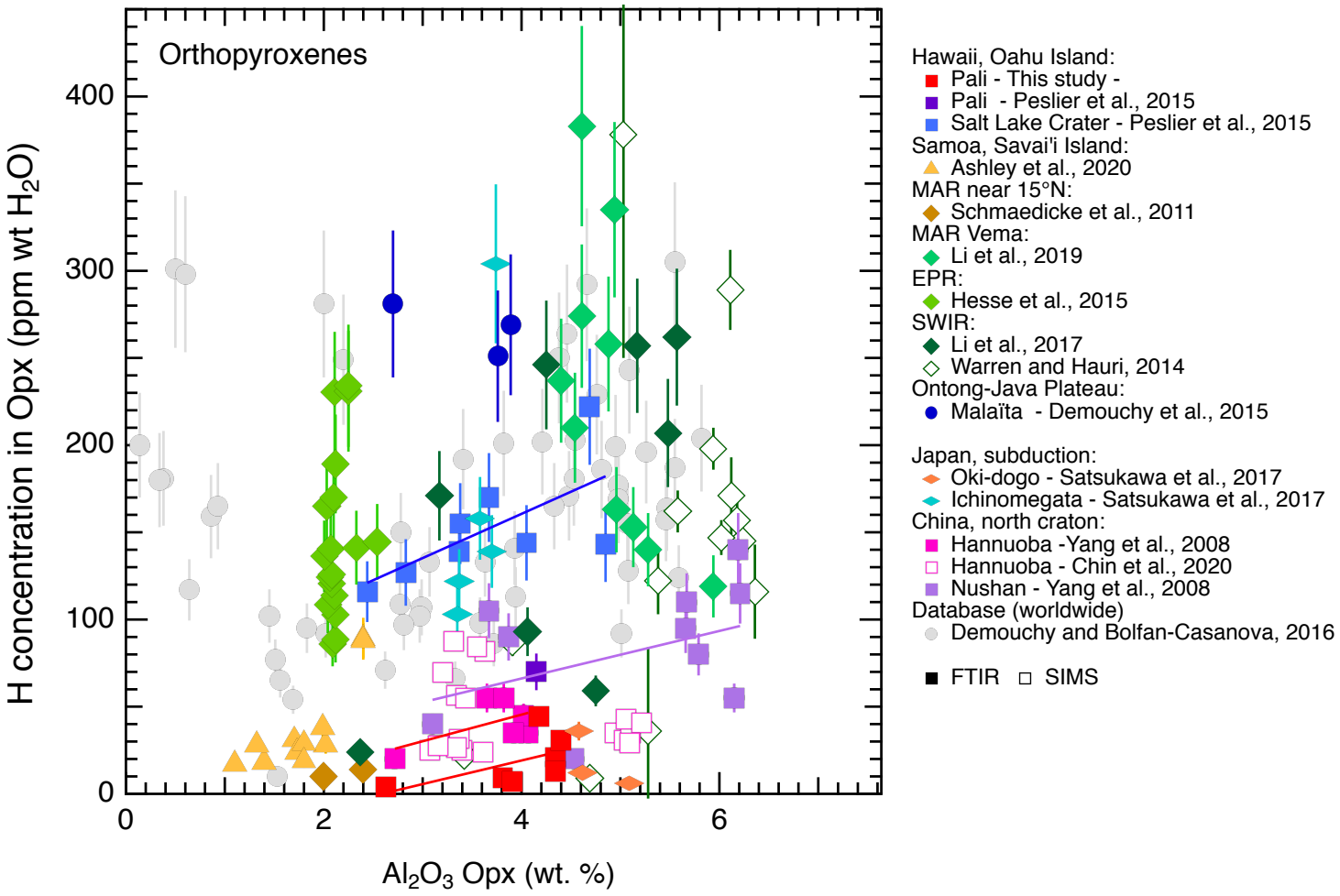

Demouchy and Tommasi, Fig. 7R

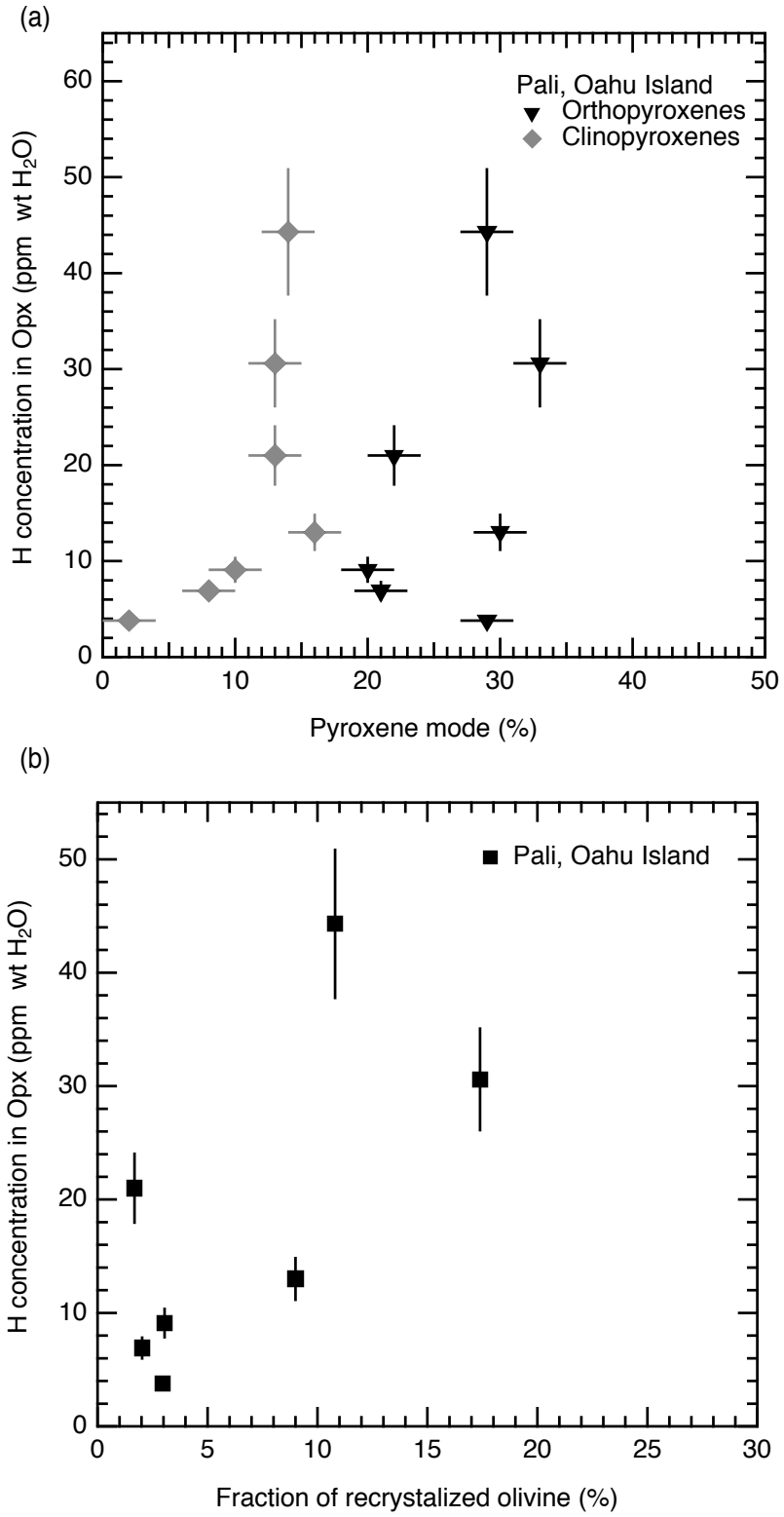

From dry to damp and stiff mantle lithosphere by reactive melt percolation atop the Hawaiian plume

S. Demouchy & A. Tommasi

Online Supplementary materials for the EPSL article:
Figures. S1, S2, S3, S4 and S5

Fig. S1: Scan of each peridotite thick section (500 μm) used for FTIR, presented together with the mineral phase map from EBSD data from Tommasi et al. (2020) acquired on regular thin section (30 μm) and map showing the grain orientation spread (GOS) of olivine. We recall that the recrystallized fraction of olivine, is olivine grains with both a grain size < 500 μm and grain orientation spread (GOS) < 1.5°) is plotted with red grain boundaries in each GOS map. See main text for details

PAL1

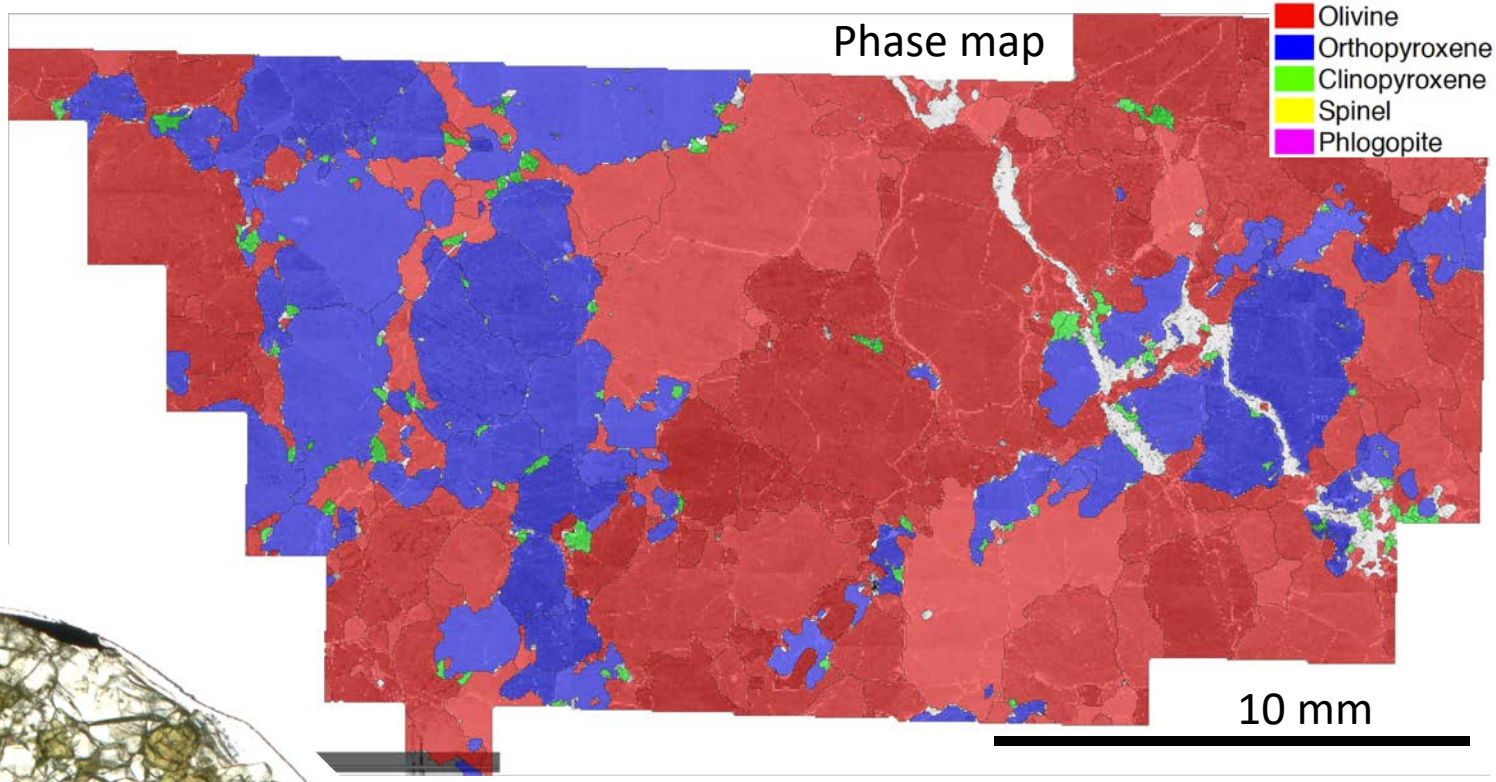

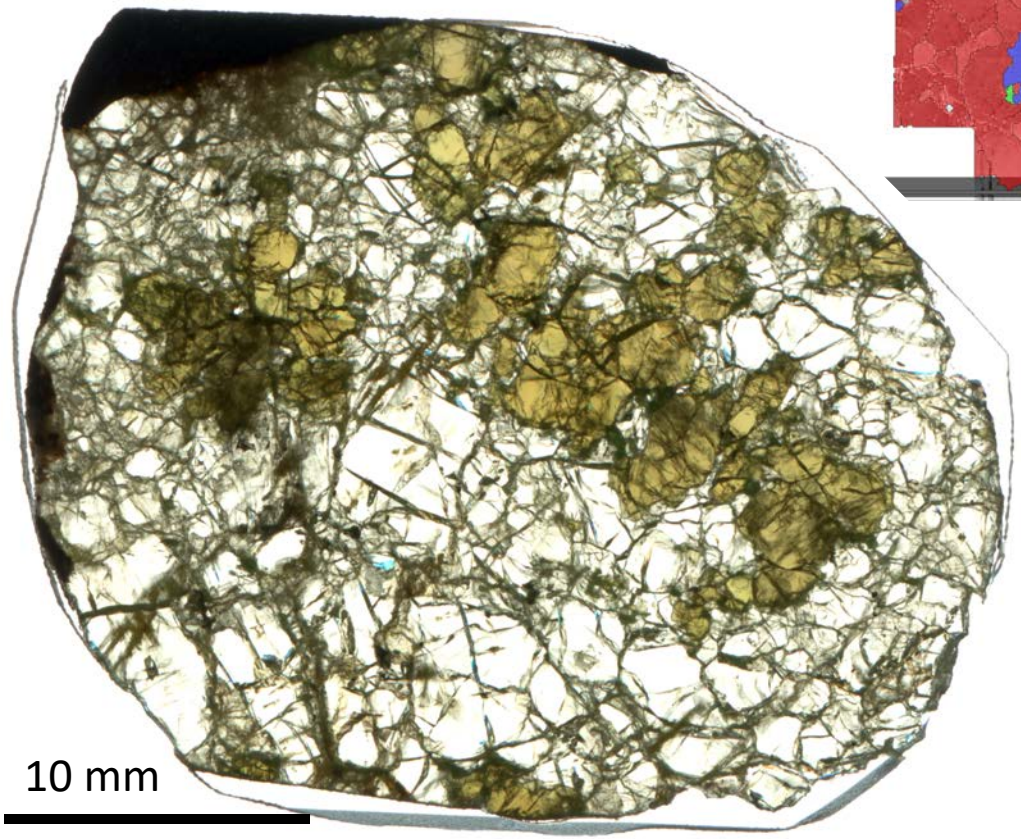

Grain orientation spread (°)

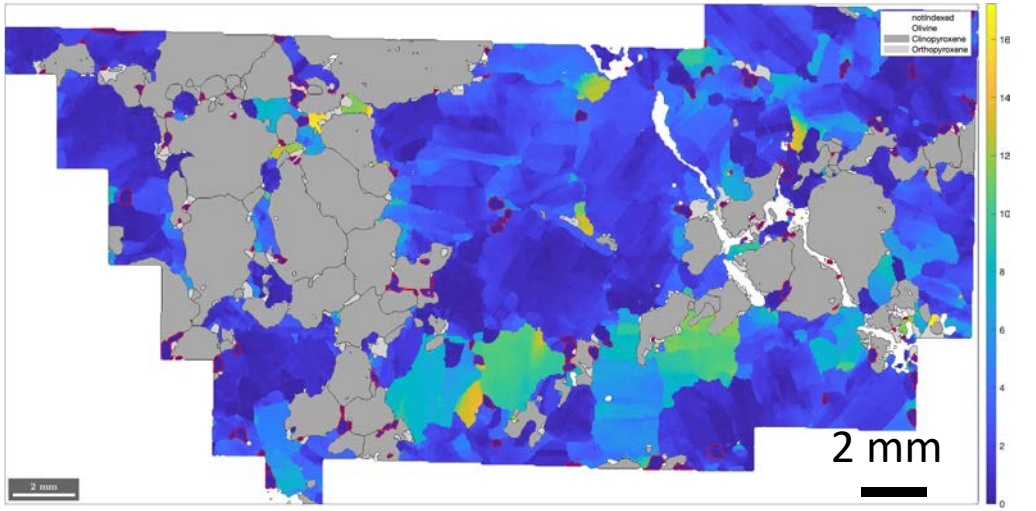

PAL3

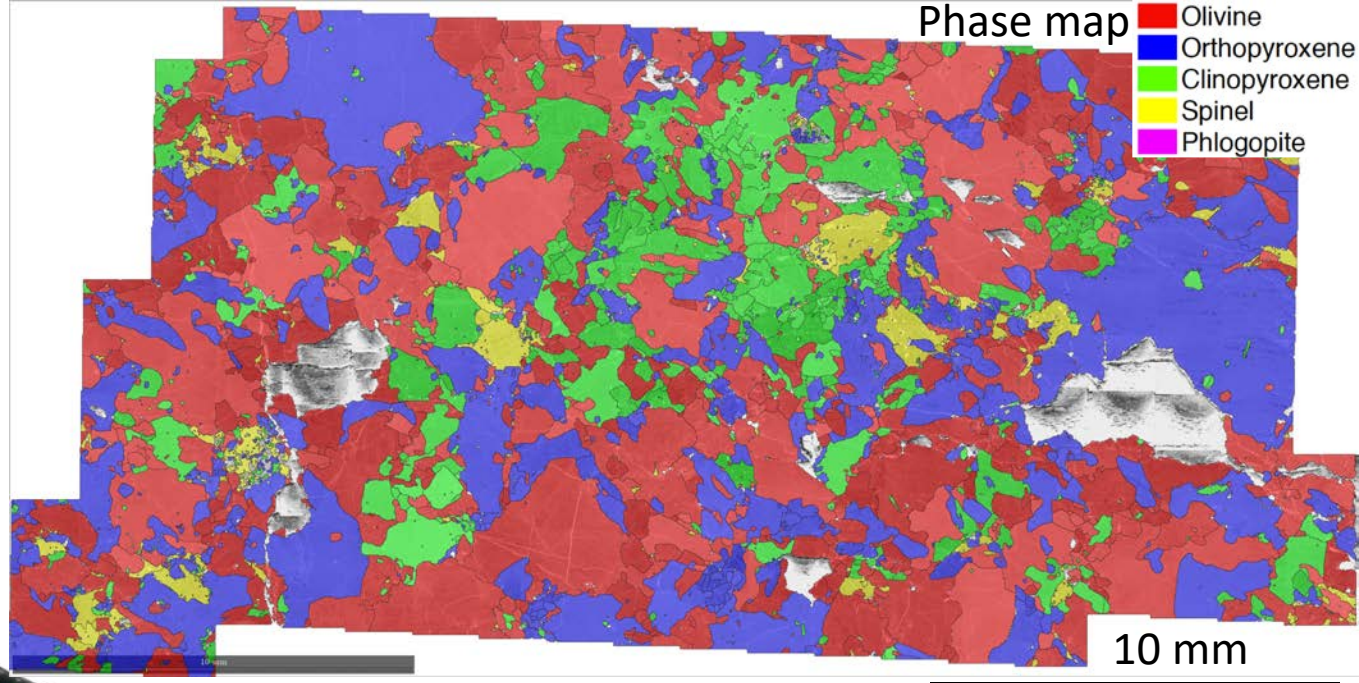

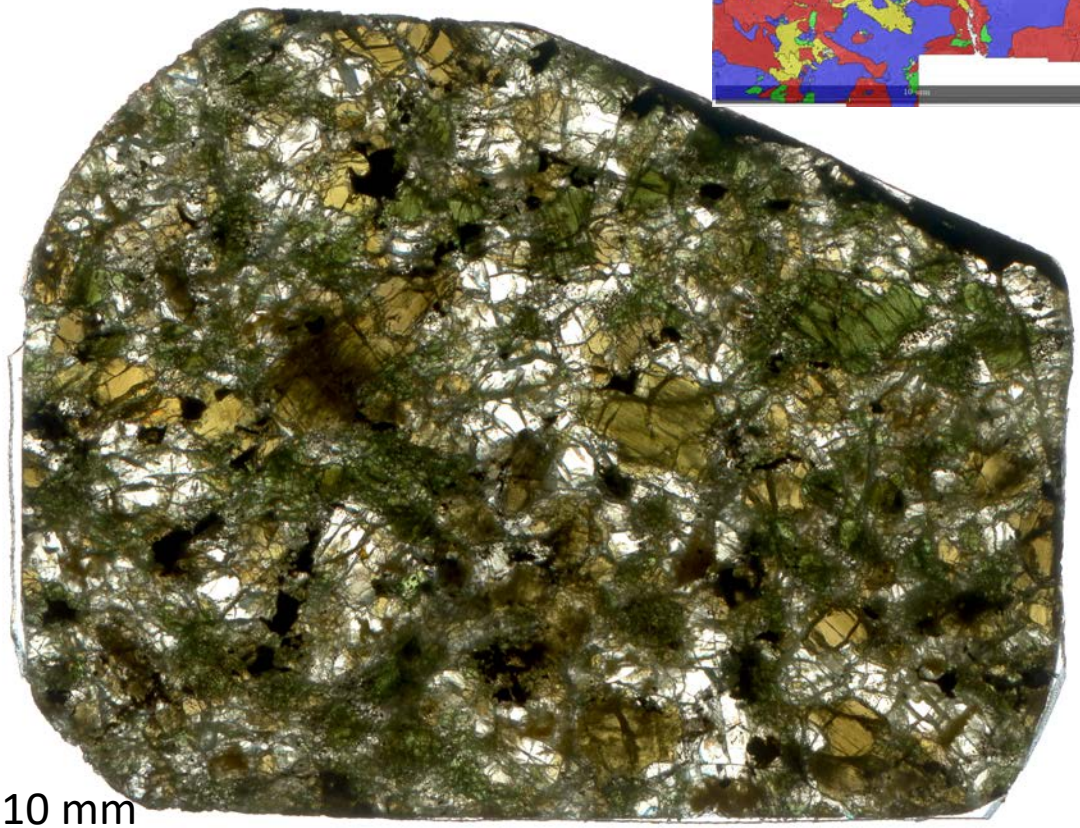

Grain orientation spread (°)

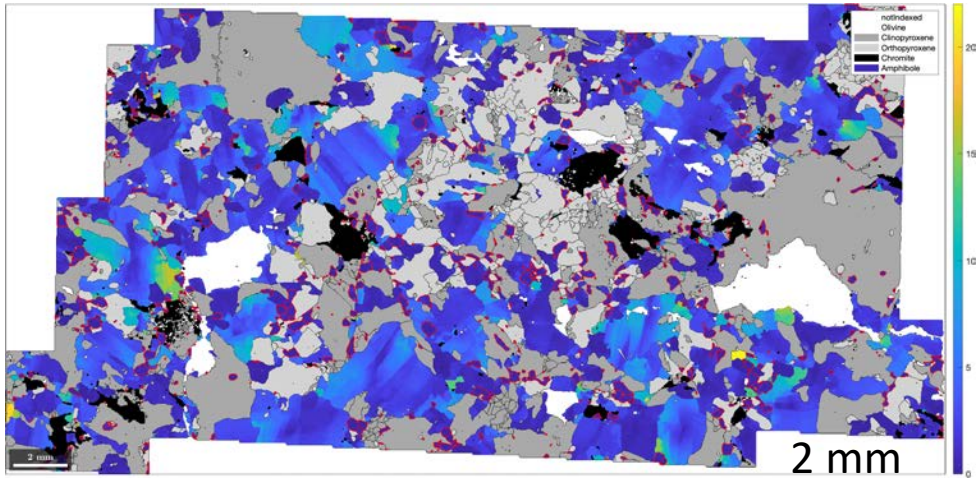

PAL7

Phase map

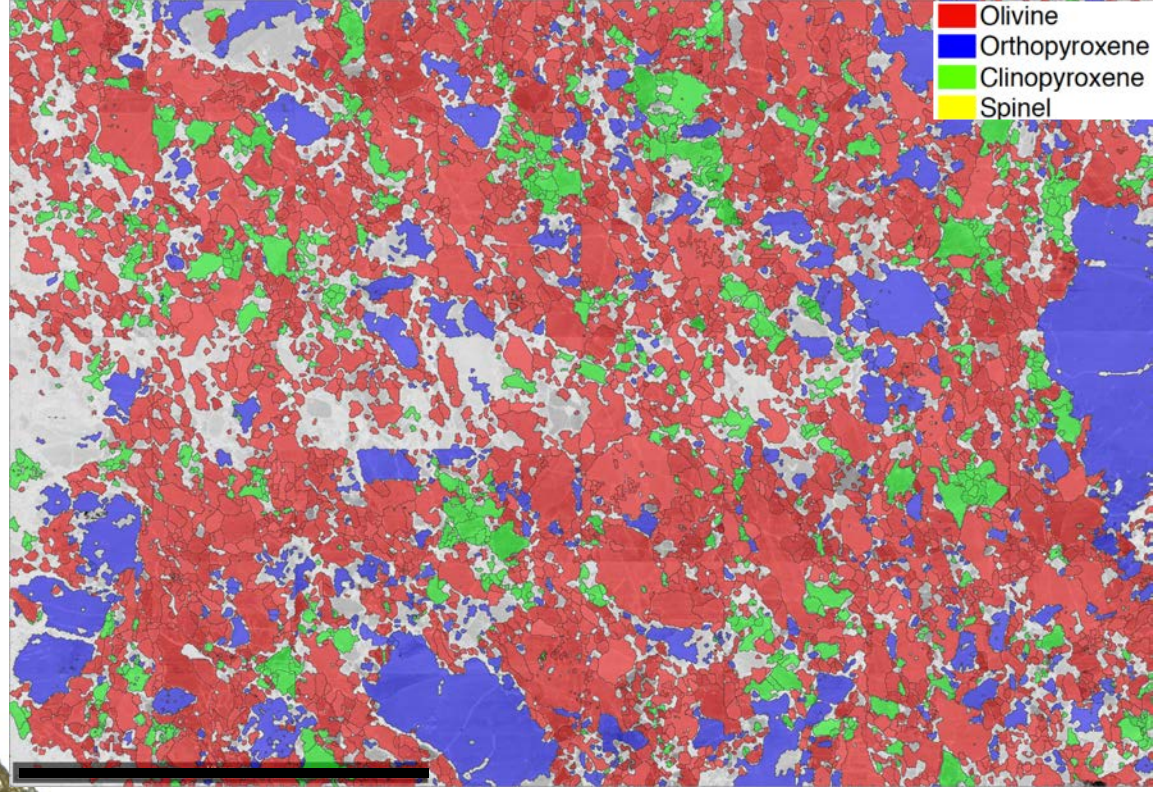

10 mm

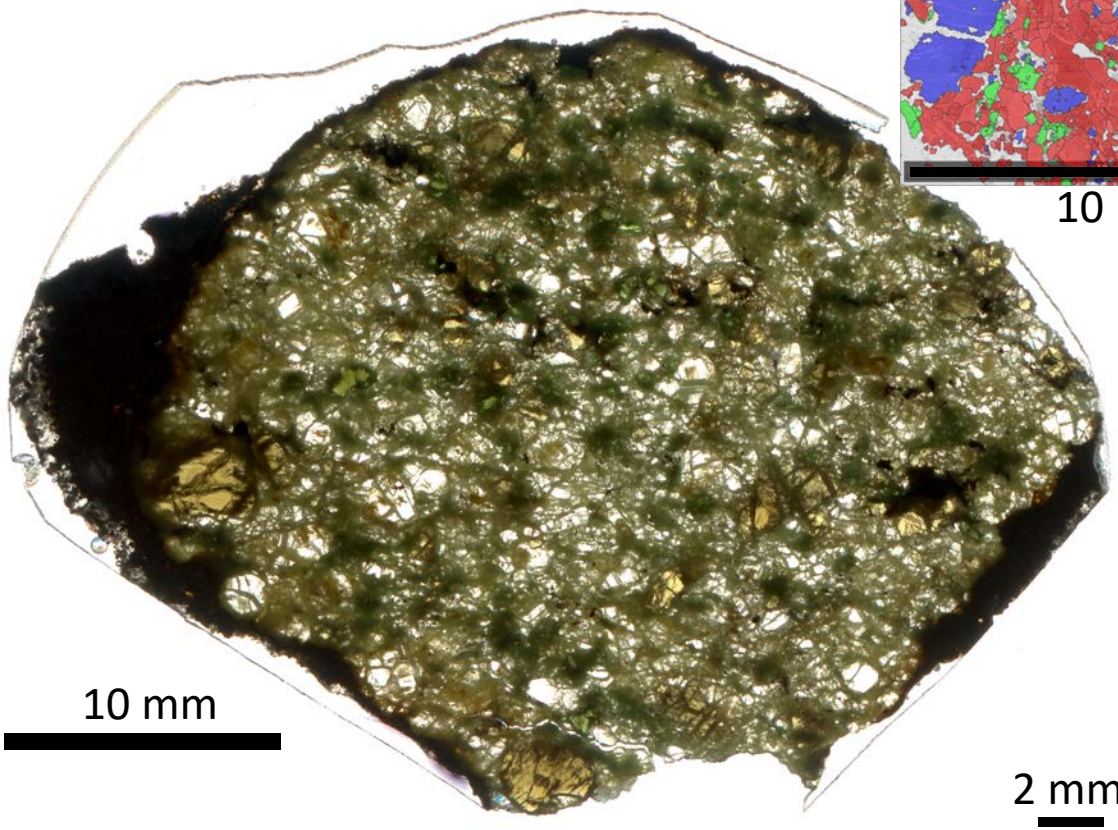

10 mm

Grain orientation spread (°)

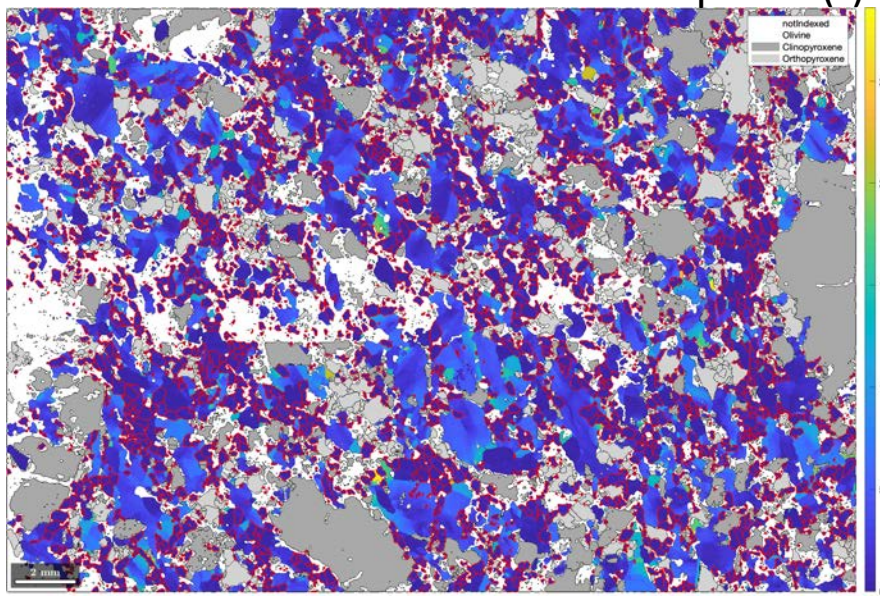

2 mm

PAL10

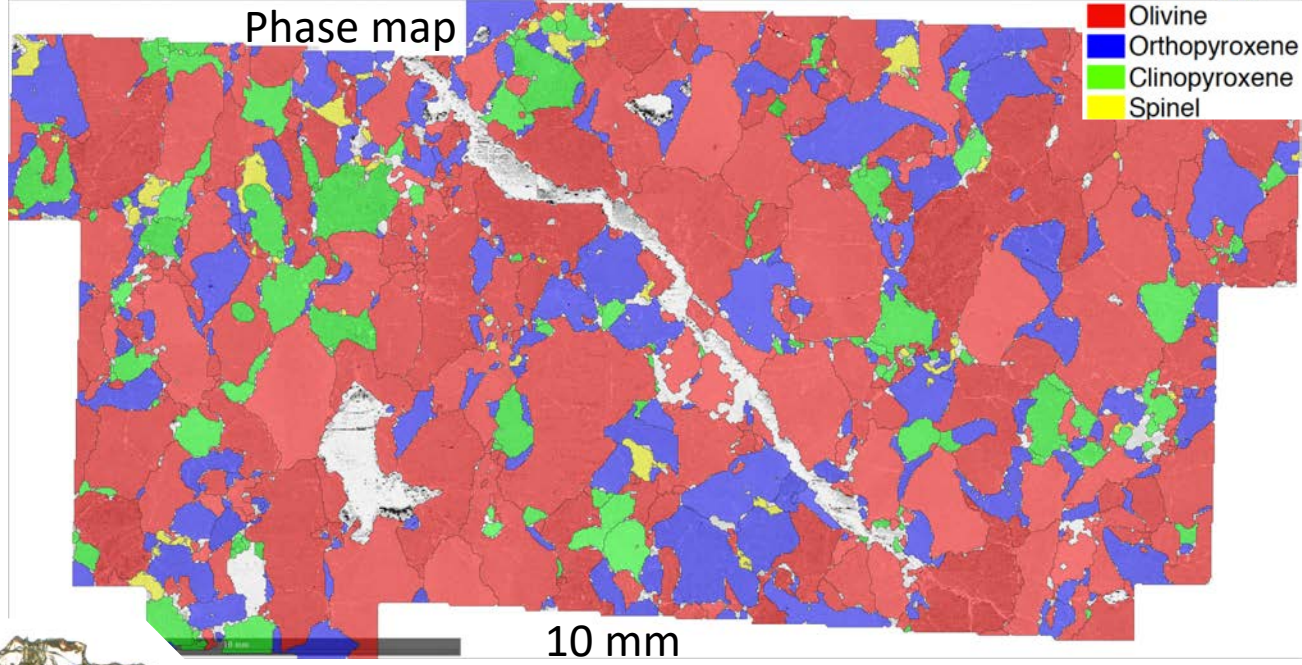

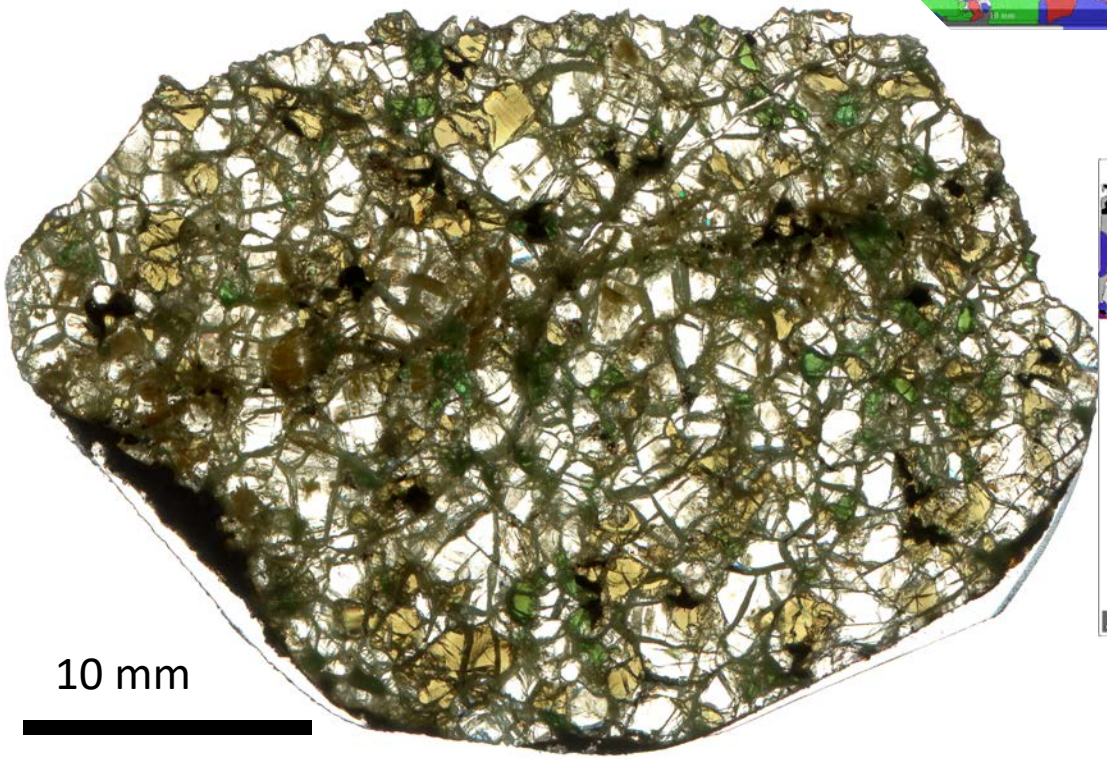

Grain orientation spread (°)

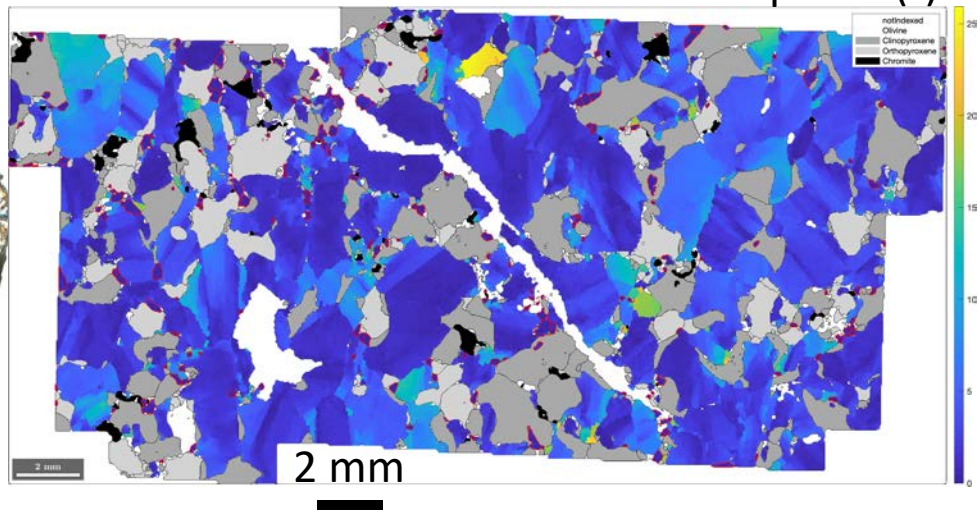

PAL12

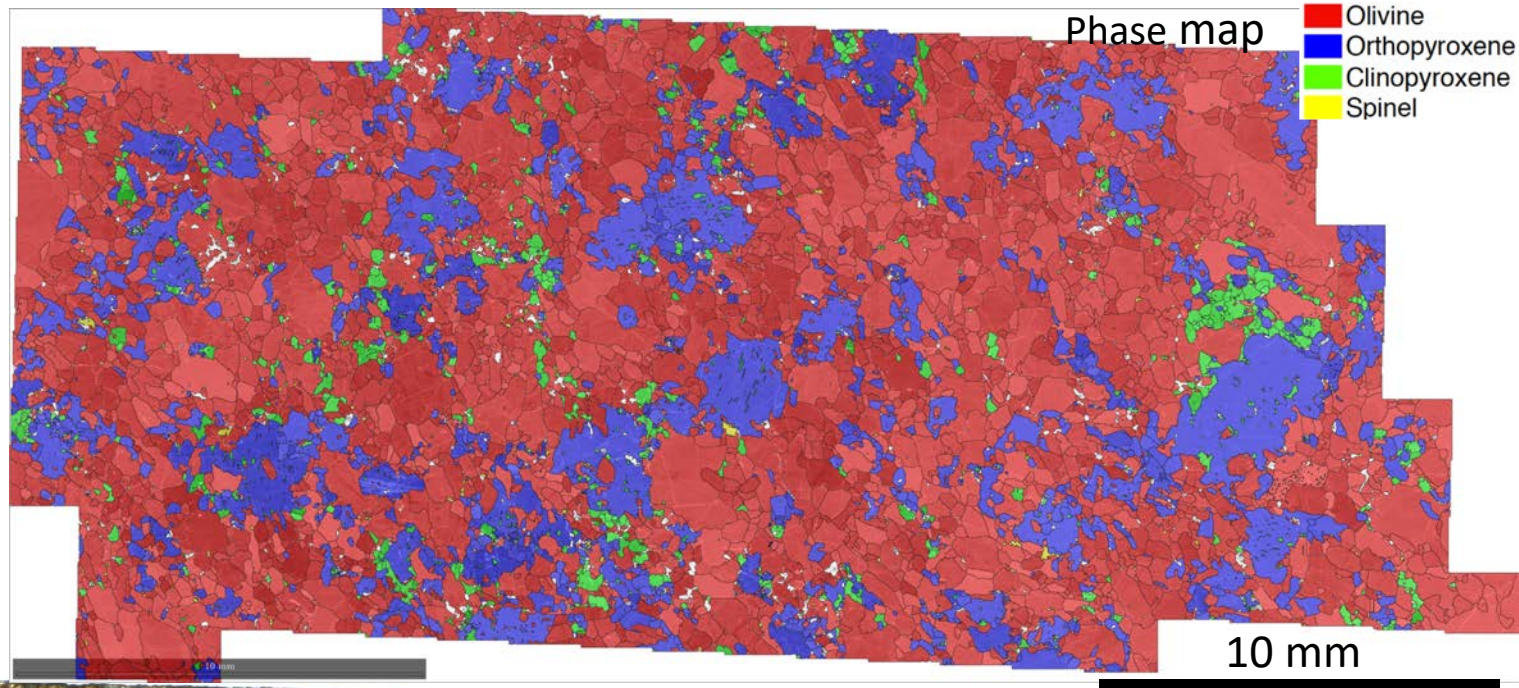

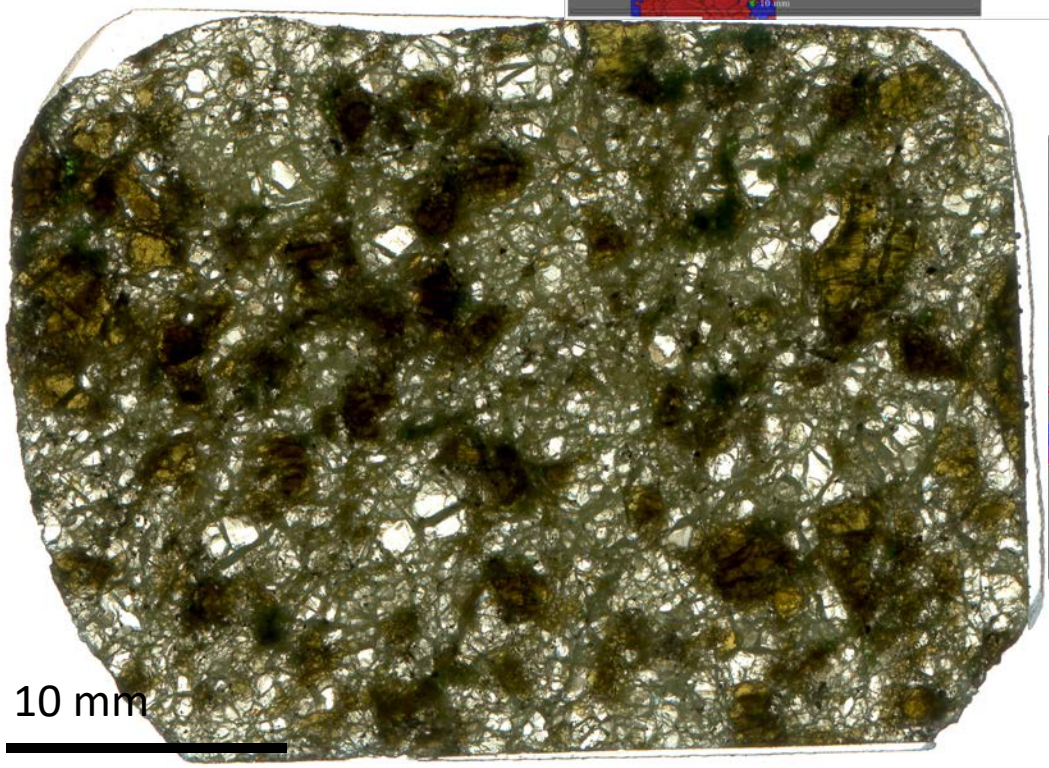

Grain orientation spread (°)

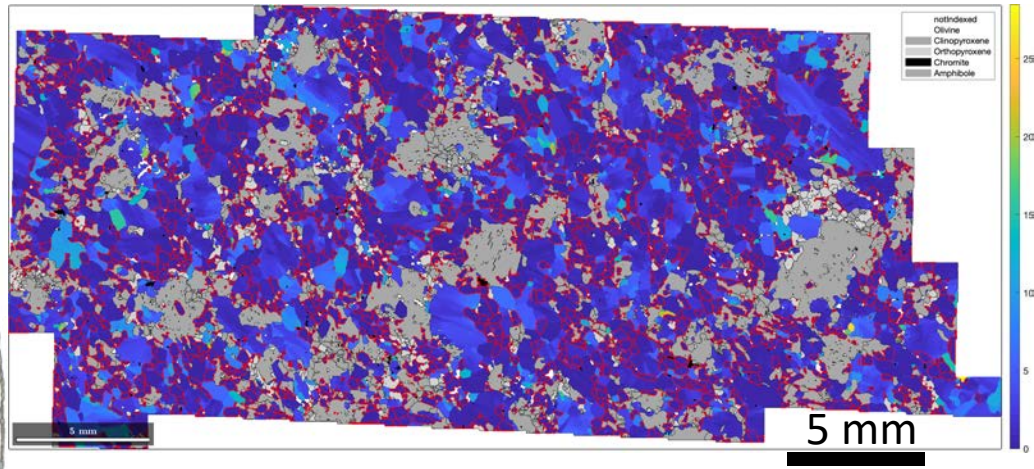

PAL18

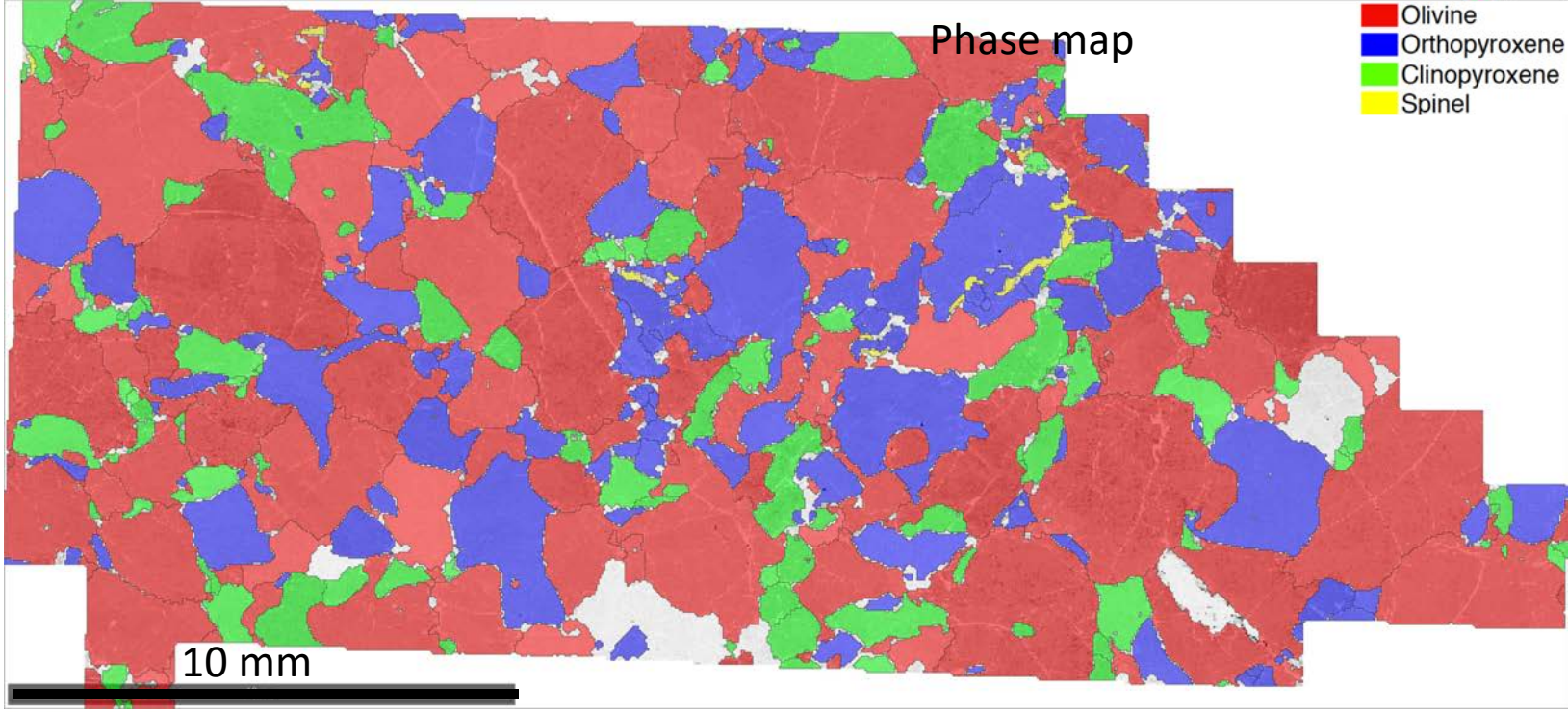

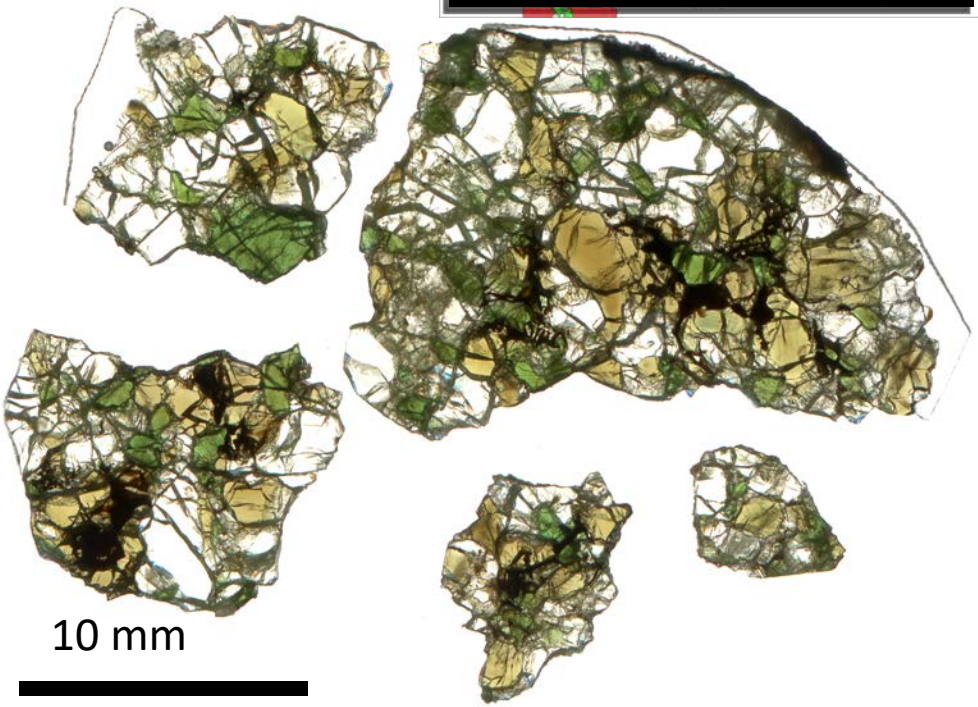

Grain orientation spread (°)

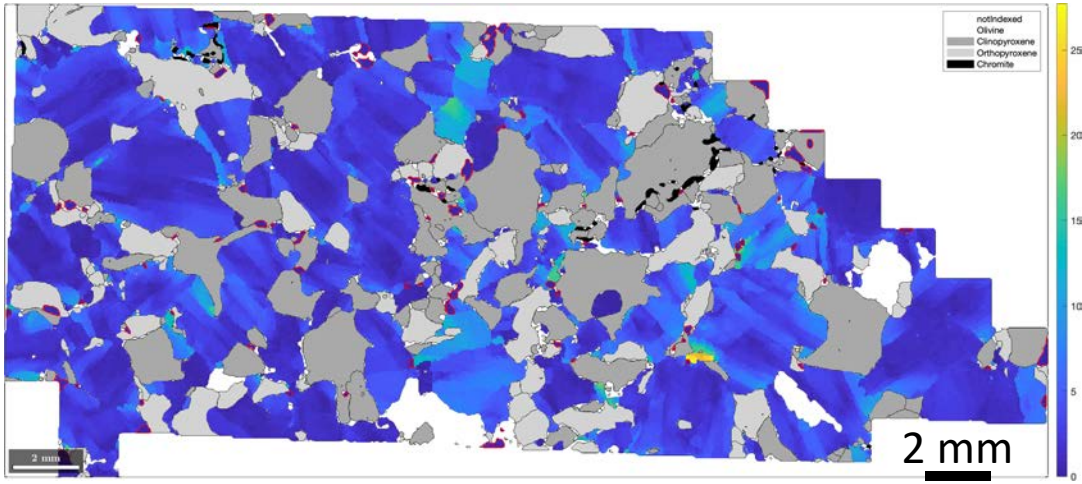

PAL23a

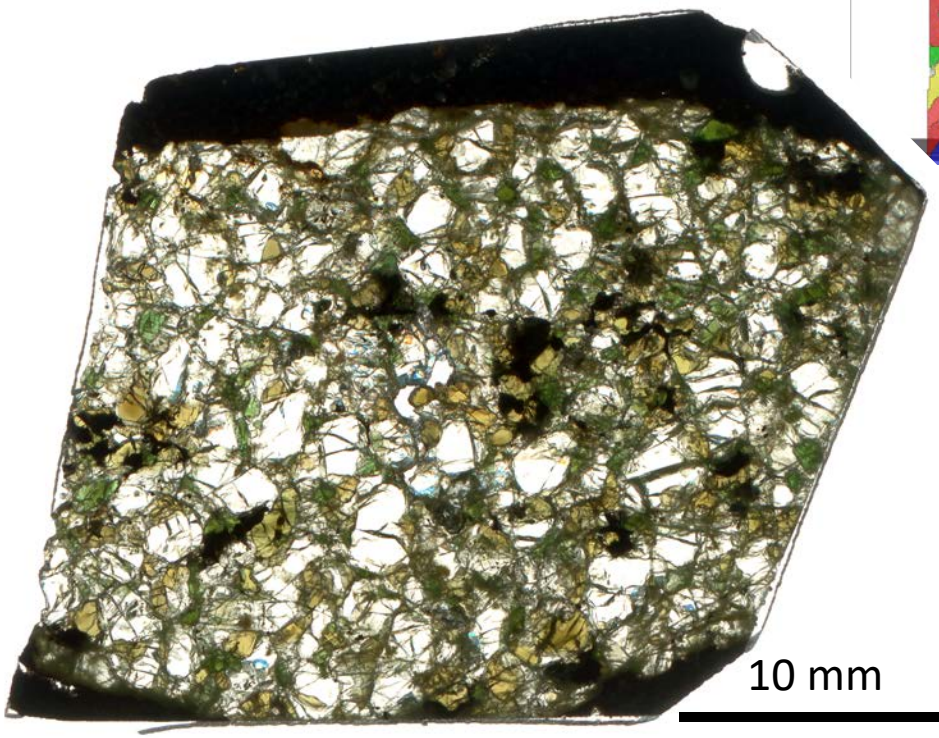
10 mm

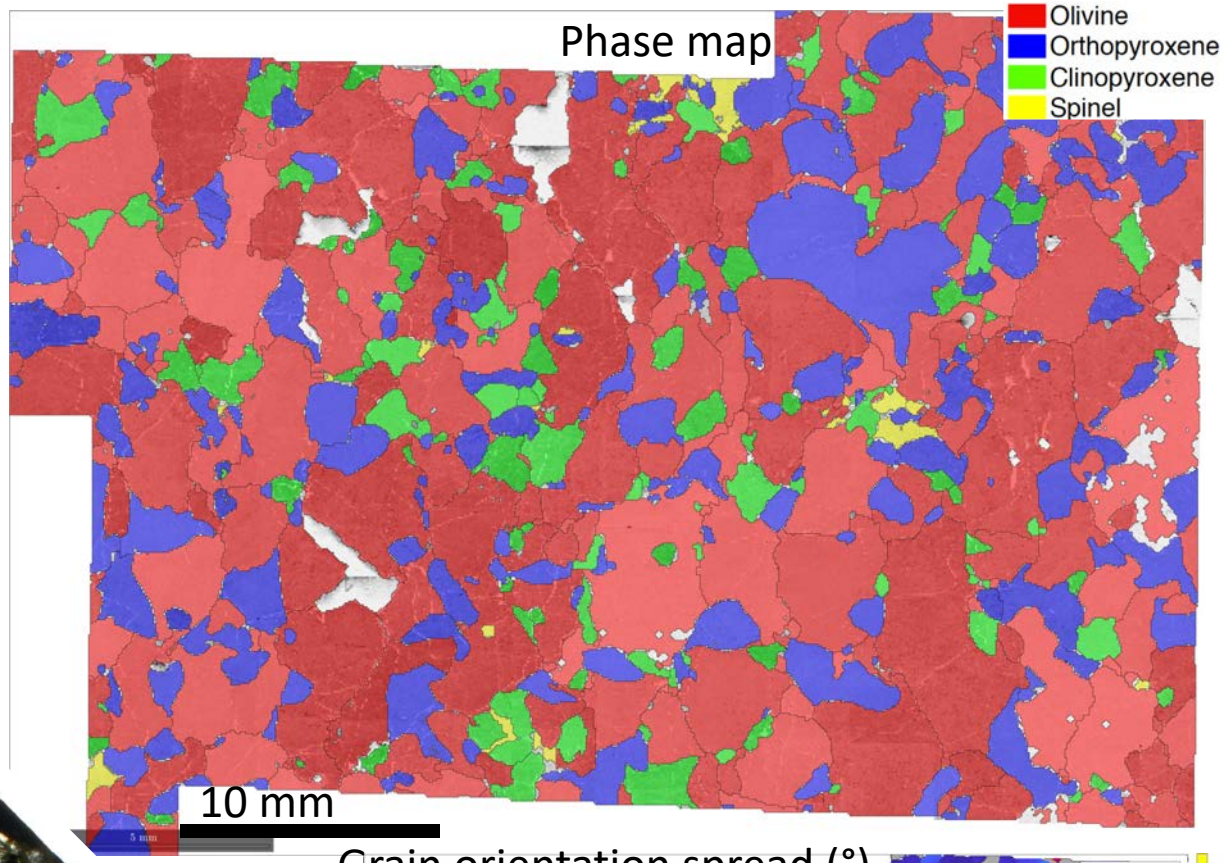
Phase map
Olivine
Orthopyroxene
Clinopyroxene
Spinel
10 mm

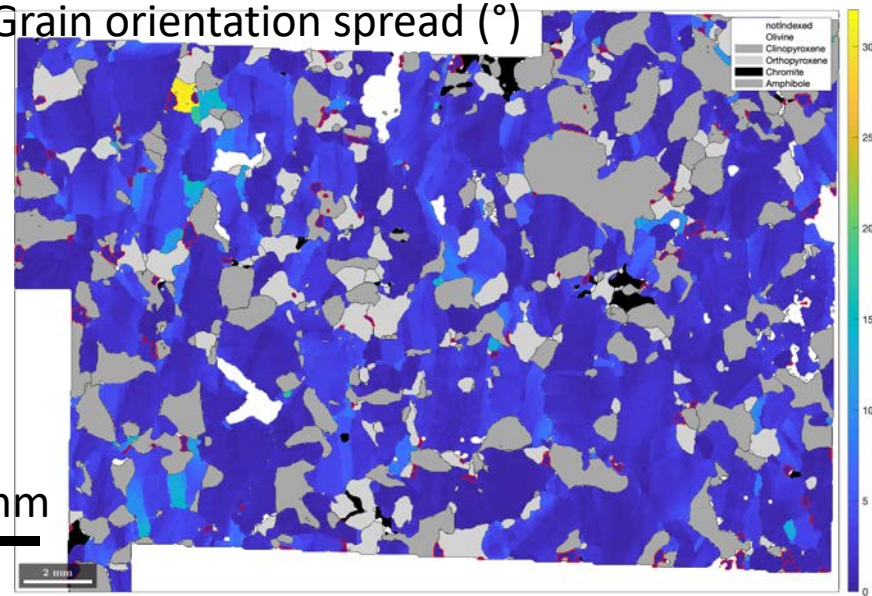
Grain orientation spread (°)
notIndexed
Olivine
Clinopyroxene
Orthopyroxene
Chromite
Amphibole
2 mm

PAL24

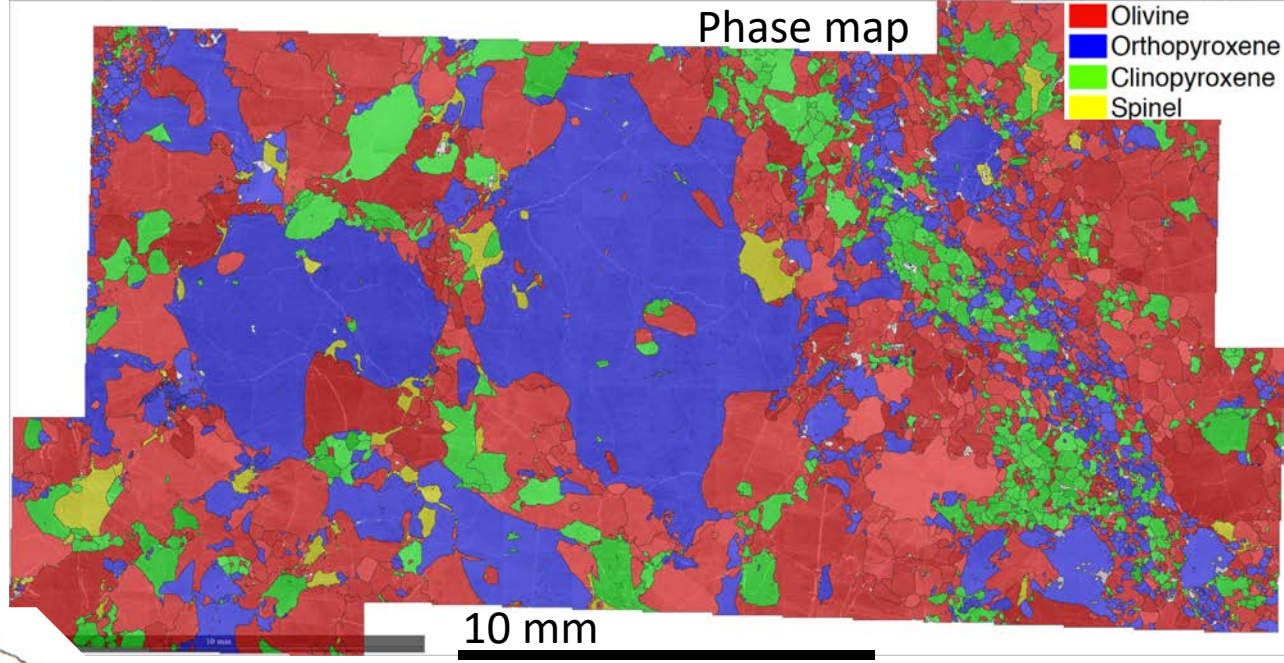

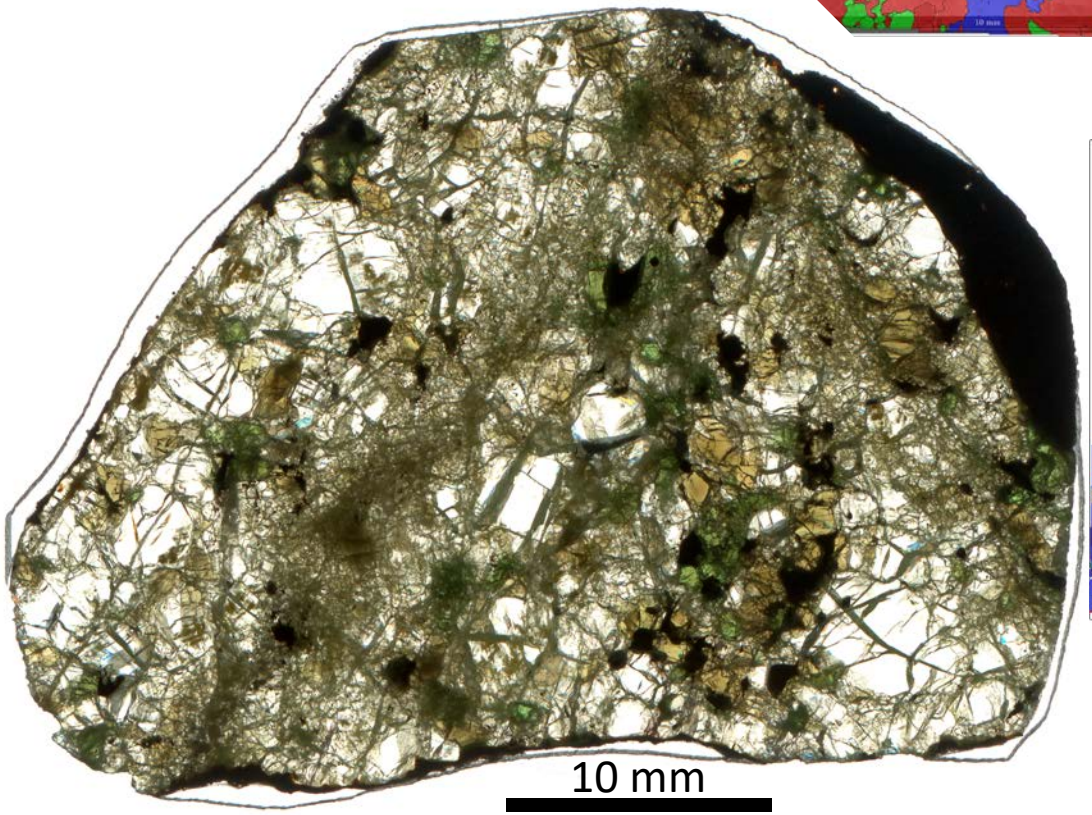

Grain orientation spread (°)

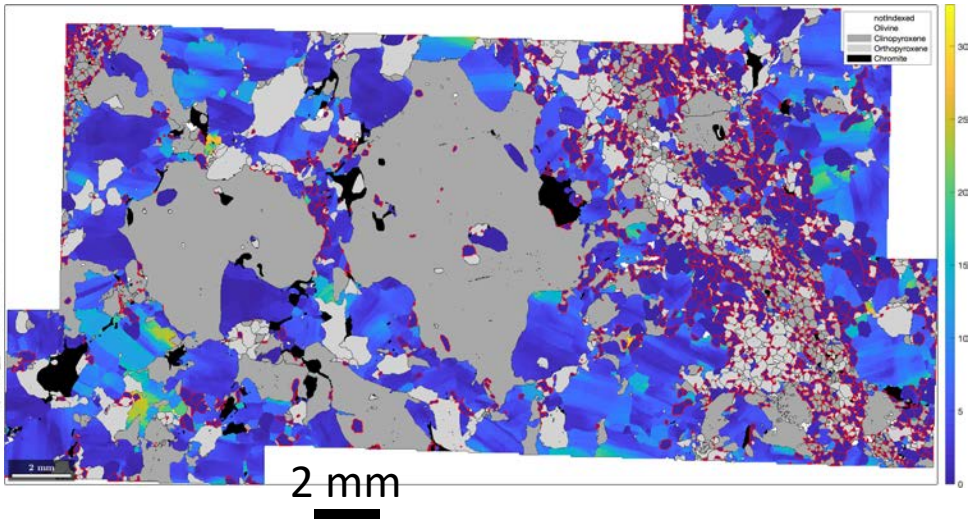

PAL25b

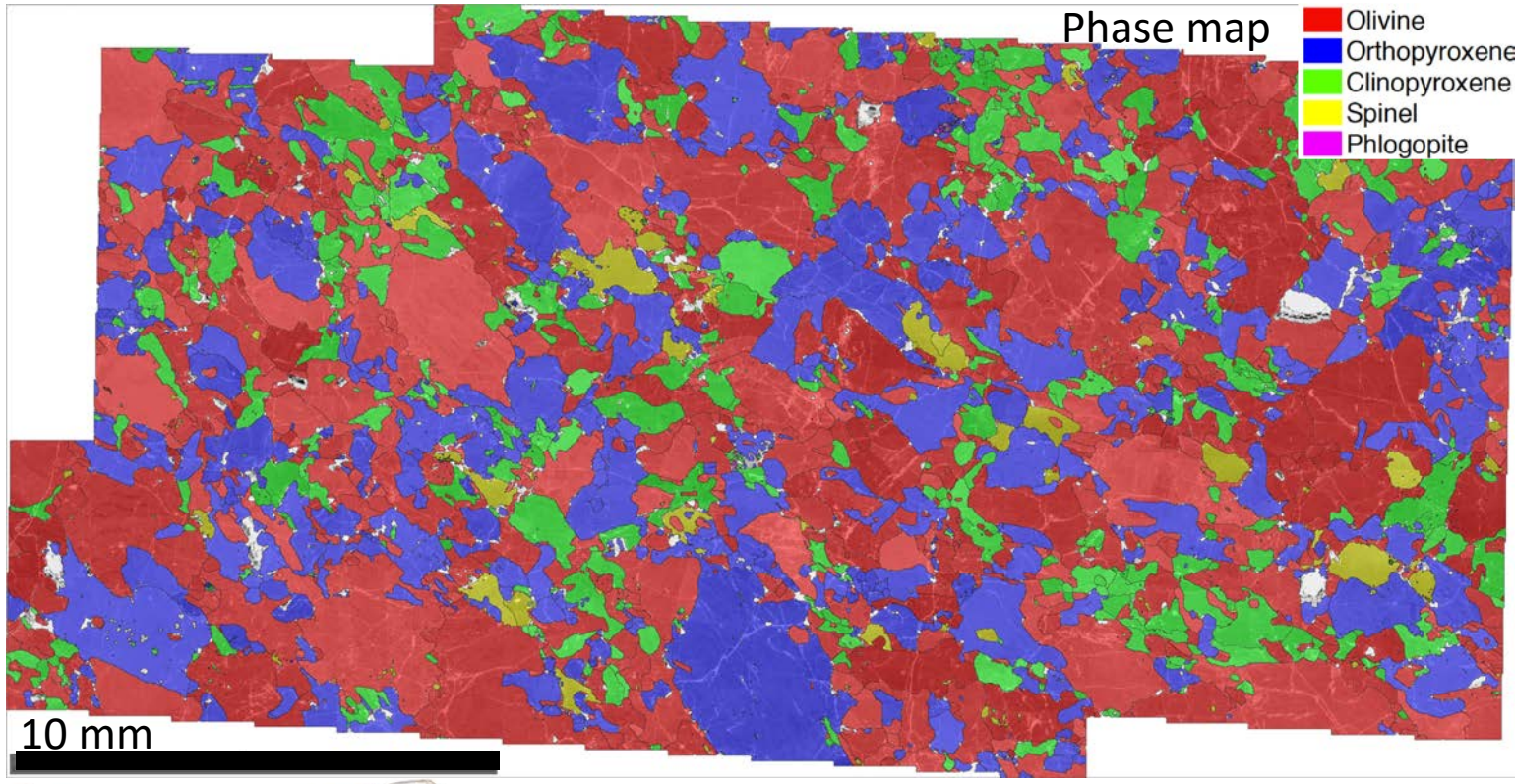

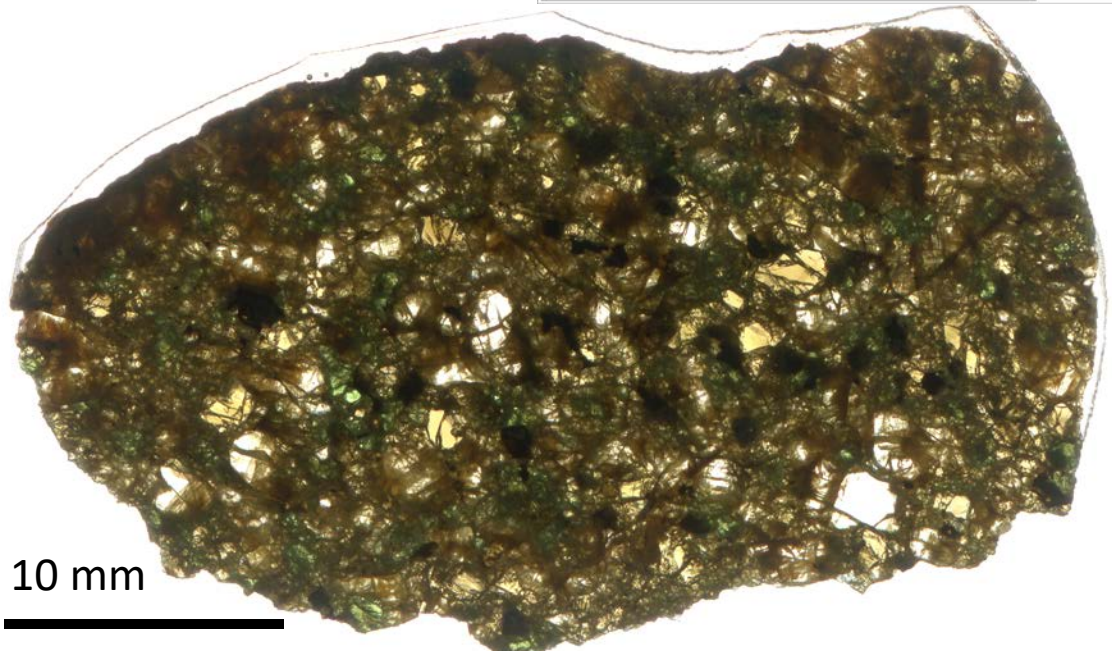

Grain orientation spread (°)

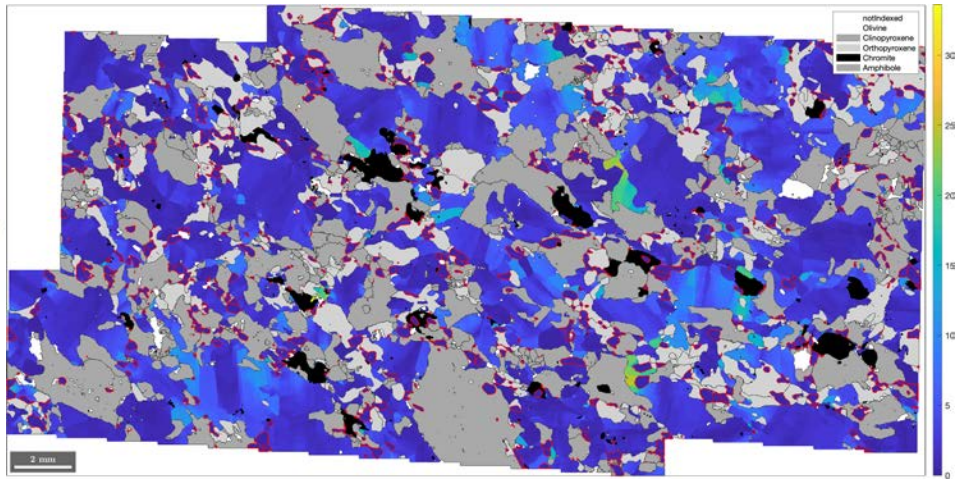

2 mm

Fig. S2: (a) Representative unpolarized infrared spectra for enstatite from this study. (b) Representative polarized infrared spectra for enstatite grain (not oriented crystallographically) from this study, which shows the shifts of the main IR bands as a function of the di-electric vector for two enstatites in PAL25B and PAL18. Spectra are offset vertically for clarity and they are all normalized to 1 cm thickness.

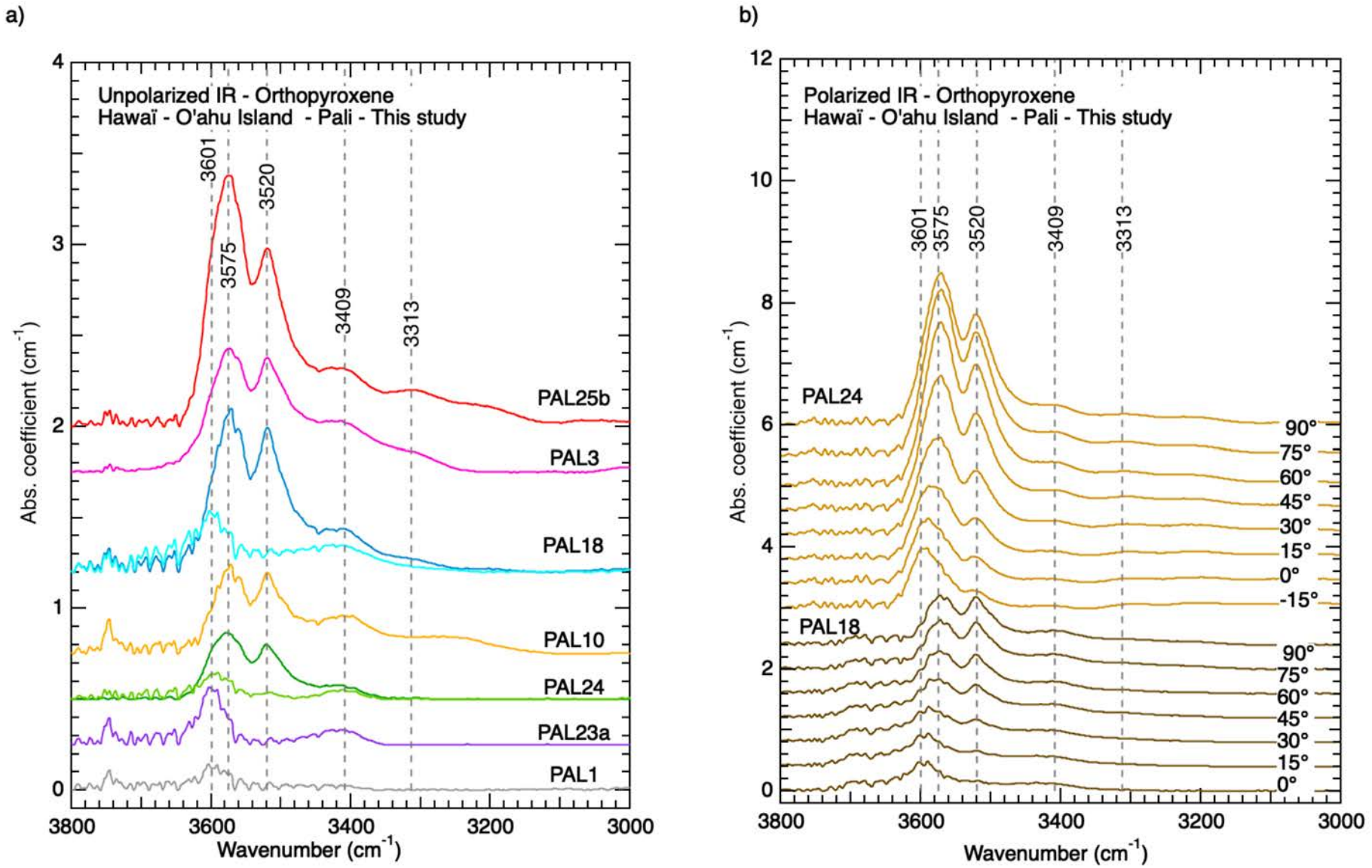

Fig. S3: (a) Photomicrographs of a clinopyroxene grain cluttered with mineral inclusions/lamellae in PAL7, and (b) corresponding unpolarized infrared spectra from this study. The spectra are normalized to 1 cm thickness.

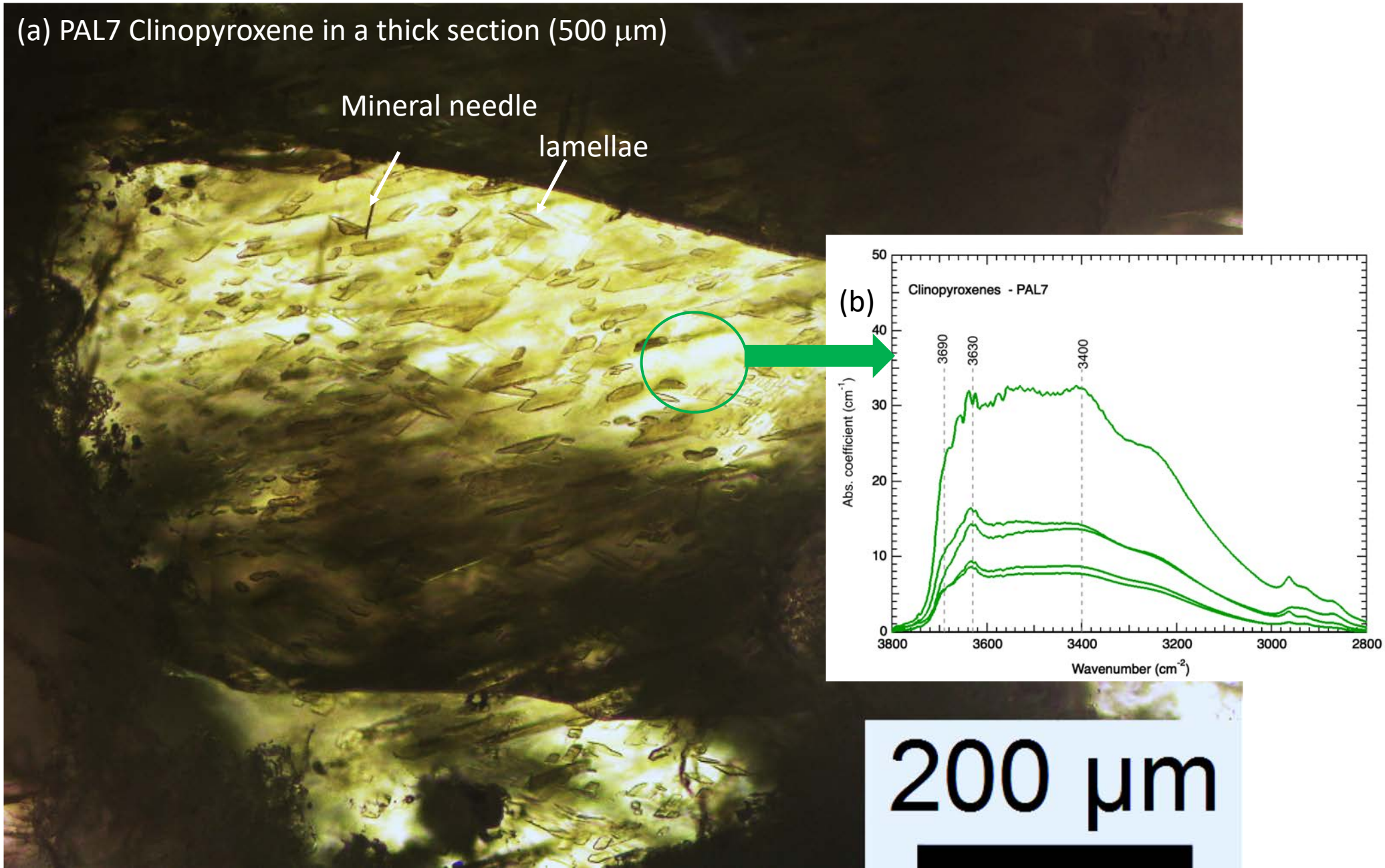

Fig. S3: (c) and (d) Photomicrographs of a orthopyroxenes grains cluttered with inclusions and lamellae in PAL12, and (e) and (f) in PAL23a.

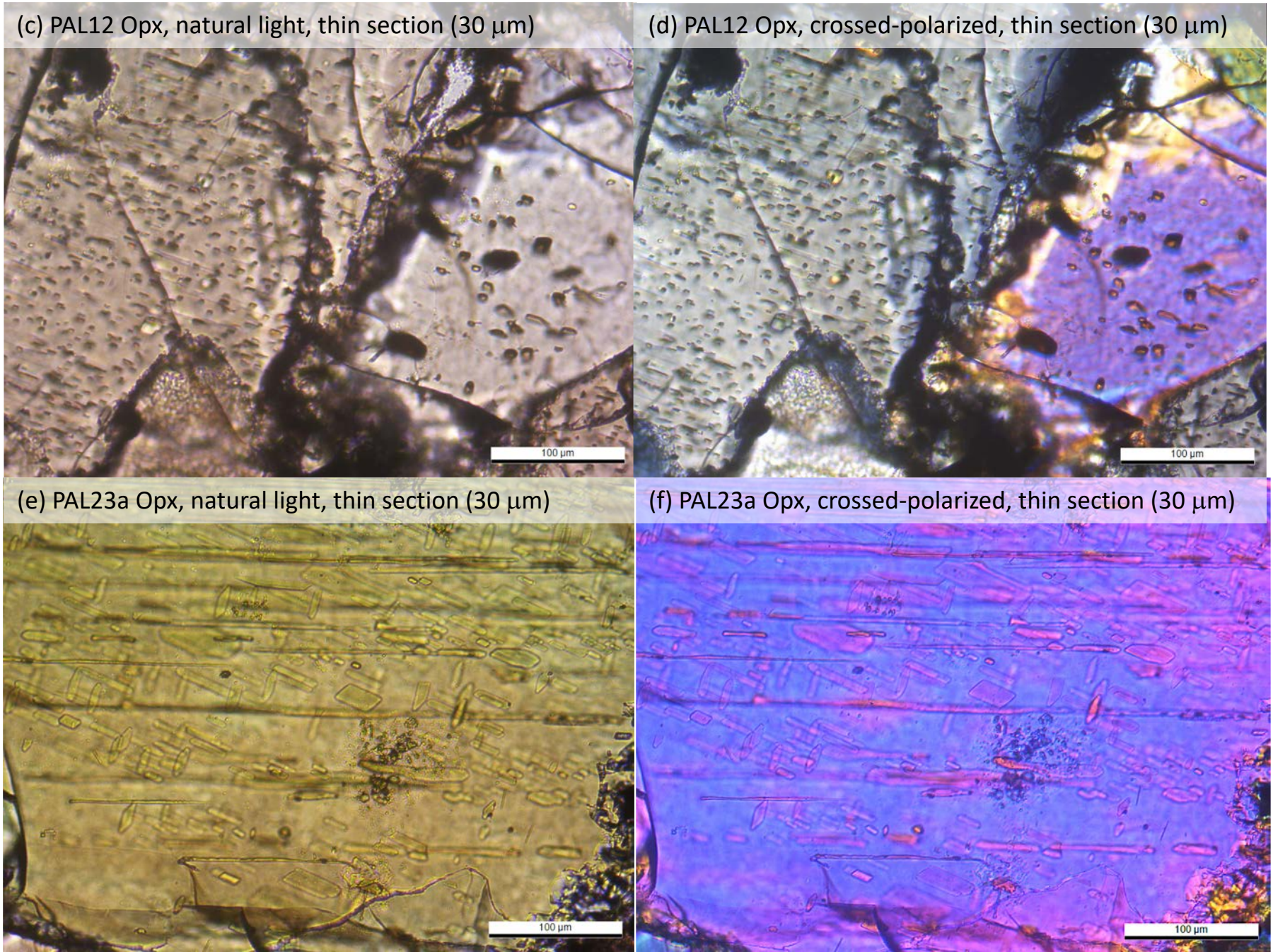

Figure S4: Forward scattered electron images of selected area in mantle minerals with lamellae inclusions presented with new electron backscatter diffraction (EBSD) maps and energy dispersive spectroscopy (EDS) maps for key elements (representative analyses from PAL7 can be found in Table S3). We recall briefly the method of acquisition. The mineralogical nature of the inclusions was determined using EBSD and EDS in a scanning electron microscope (CamScan X500FE CrystalProbe) at Geosciences Montpellier (France). No carbon coating was applied on the surface of the thin section. Working distance was 25 mm, tilt angle was 70°, acceleration voltage was 20 V and the beam current was 10 nA for EBSD map acquisition (step size ranging from 0.2 to 0.7 μm), down to 5 nA for forward scatter electron (FSE) imaging. In all cases, the following phases were listed prior to detection: forsterite ($(Mg)_2SiO_4$), diopside ($CaMgSi_2O_6$), enstatite ($(Mg,Fe)SiO_3$), spinel ($MgAl_2O_3$), chromite ($(Fe,Mg)Cr_2O_4$), magnetite (Fe_2O_3), rutile (TiO_2), ilmenite ($FeTiO_3$), chlorite $(Fe,Mg,Al)_6(Si,Al)_4O_{10}(OH)_8$ and hornblende ($(((Ca,Na,K)_2(Mg,Fe^{2+},Fe^{3+},Al)_5\ [Si_6(Al,Si)_2O_{22}](OH,F)_2$). For EDS, the following elements were detected: O, Si, Mg, Fe, Ni, Co, Cr, Mn, Al, Ca, Na and Ti. EBSD data was acquired with the Oxford instruments HKL Aztec2 software and further treated with the Tango. Data treatment consist in removing wild spikes and filled non-indexed pixels when 7 neighbors with identical orientations were present.

Figure S4a: PAL12: Site 1, Orthopyroxene with Cr-spinel and diopside lamellae
Step size of the EBSD map: 0.2 µm

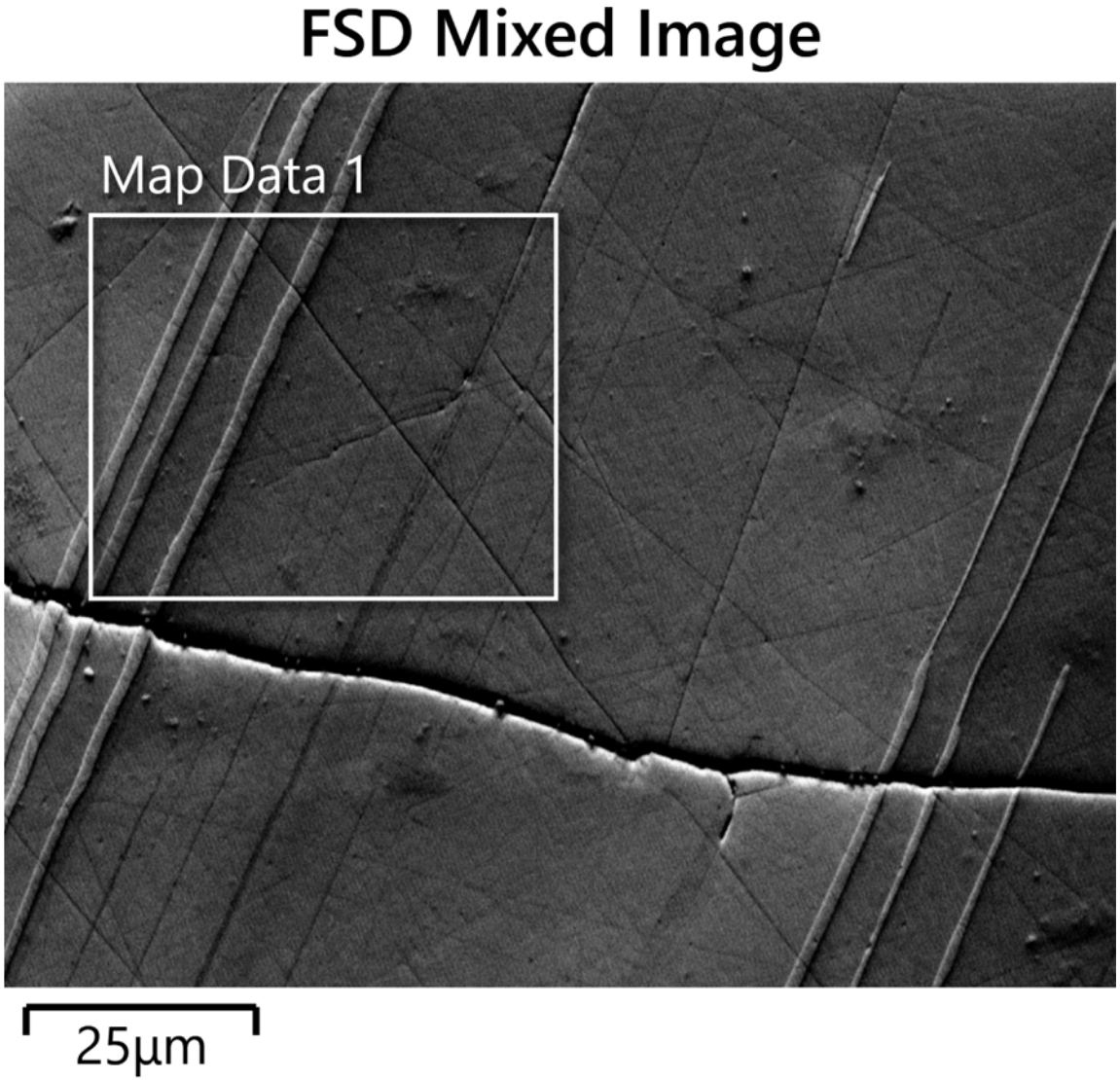

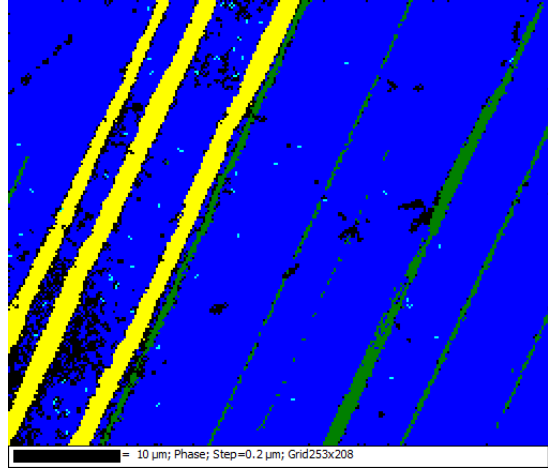

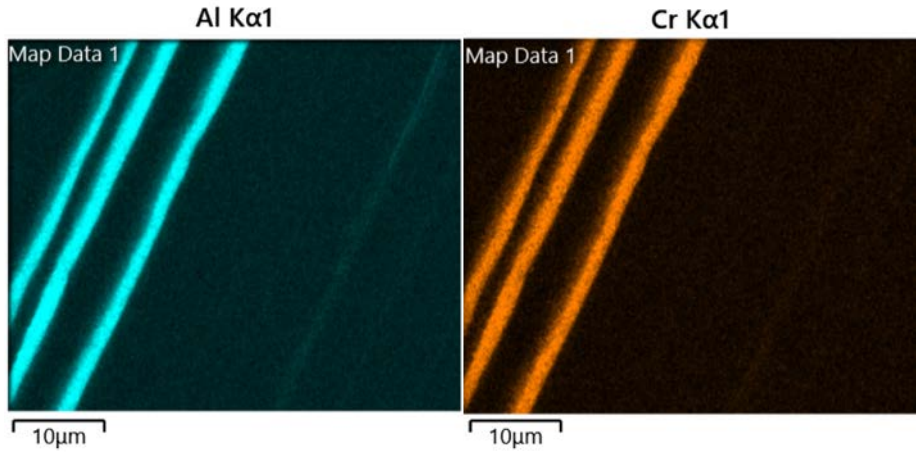

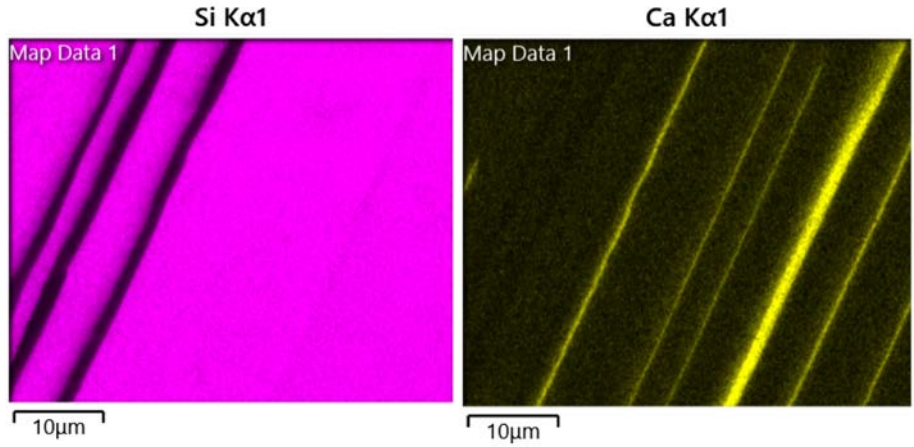

Figure S4b: PAL12: Site 7, Orthopyroxene with diopside lamellae. Step size of the EBSD map: 0.7 µm

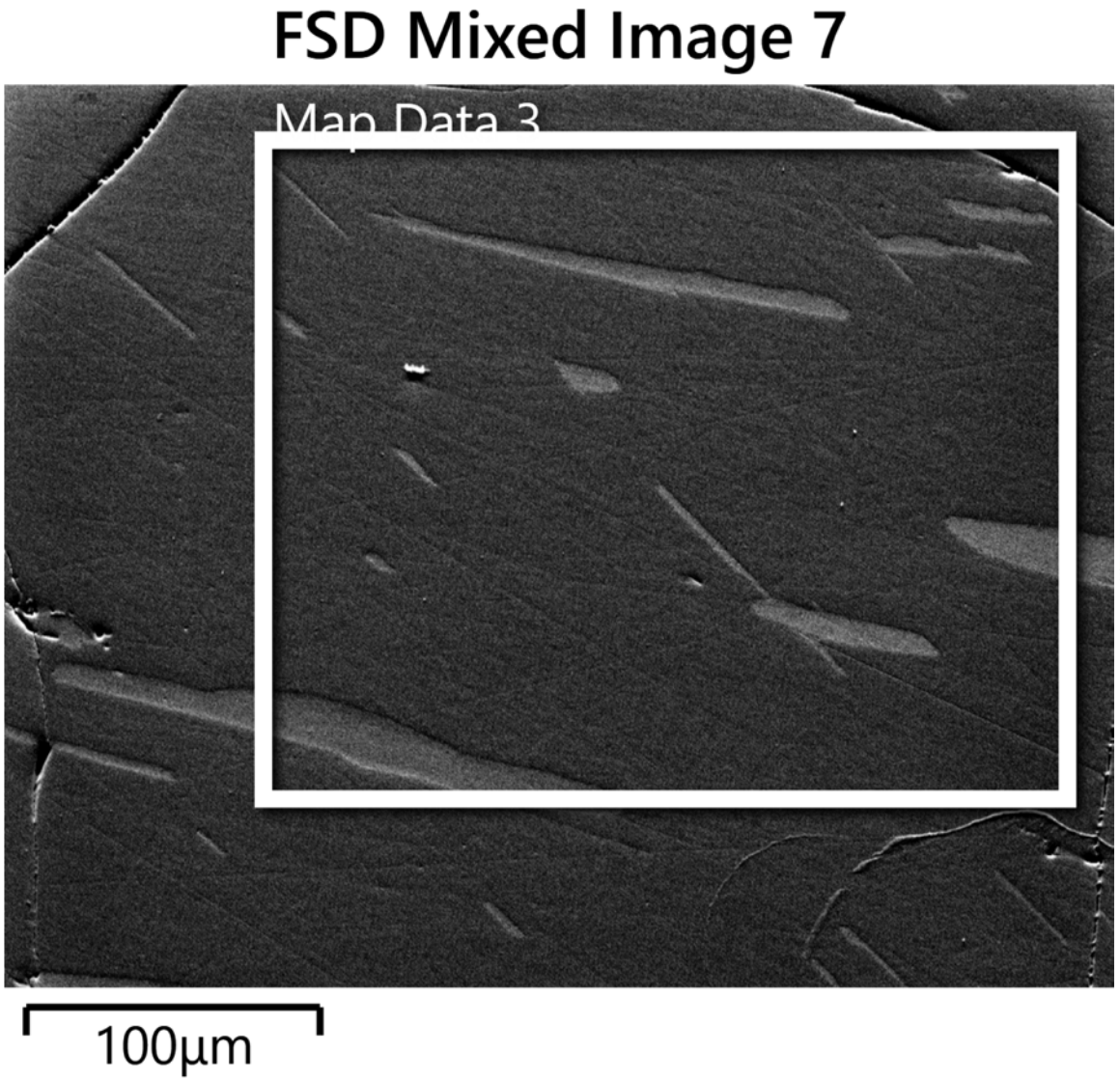

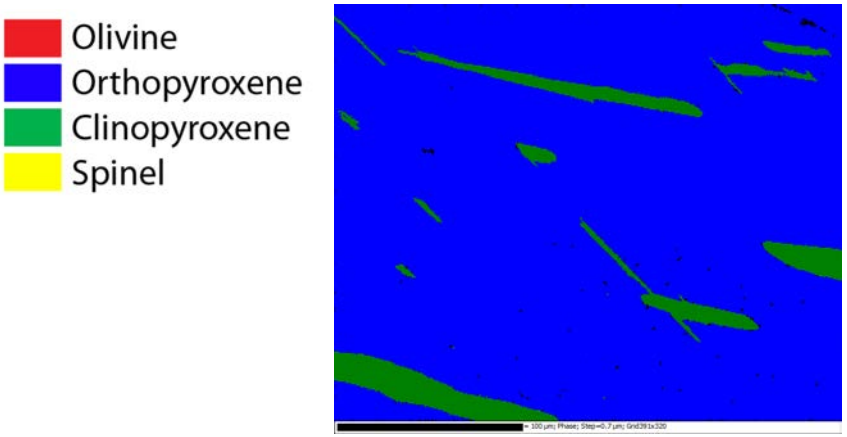

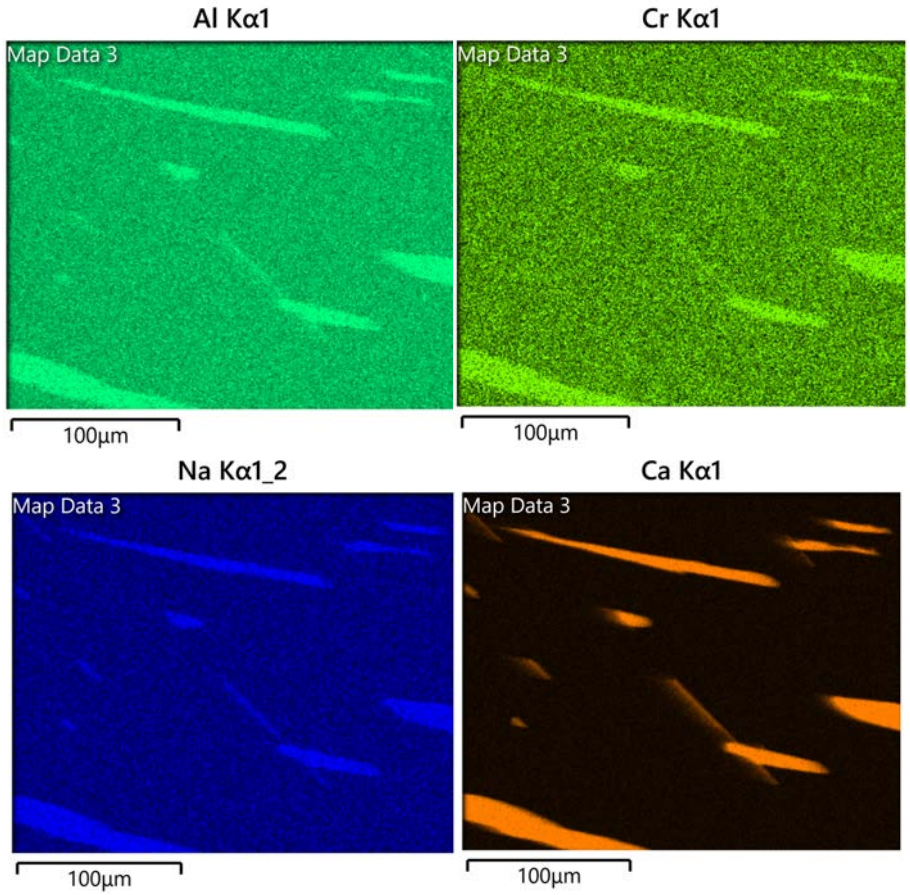

Figure S4c: PAL12: Site 8, Orthopyroxene with Cr-spinel and diopside lamellae
Step size of the EBSD map: 0.3 µm

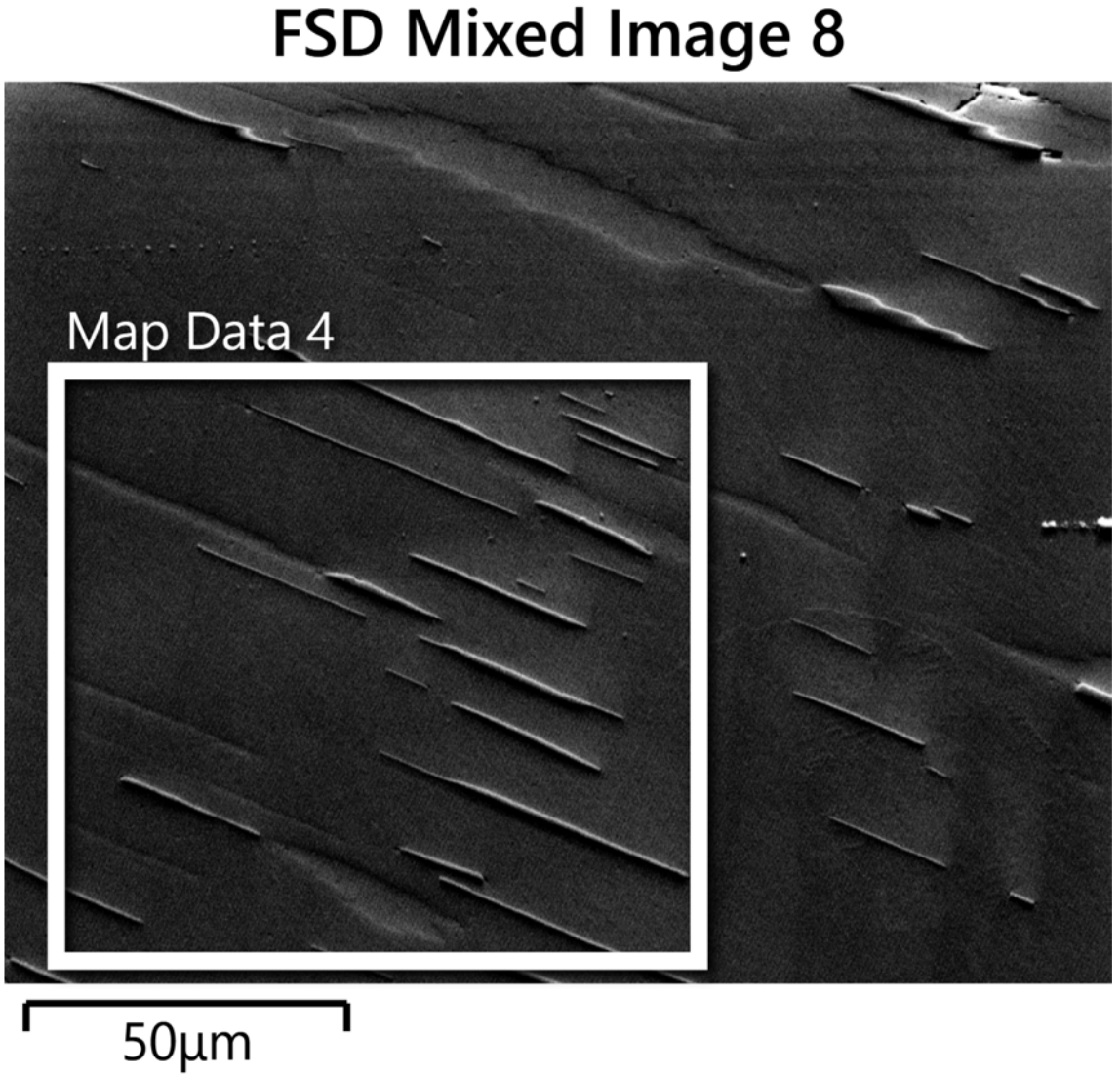

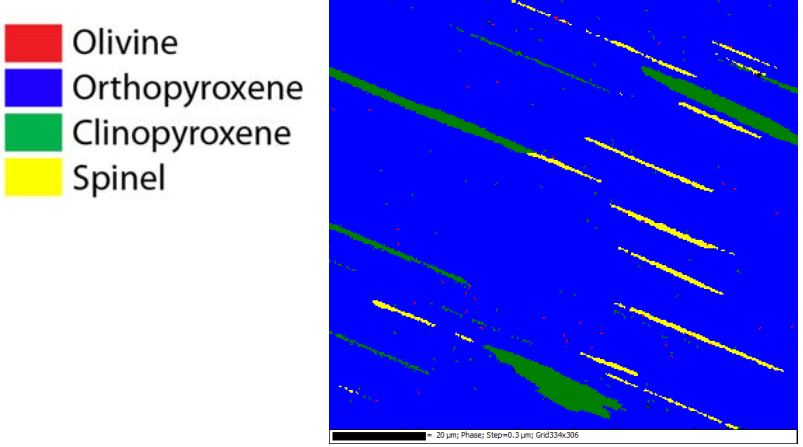

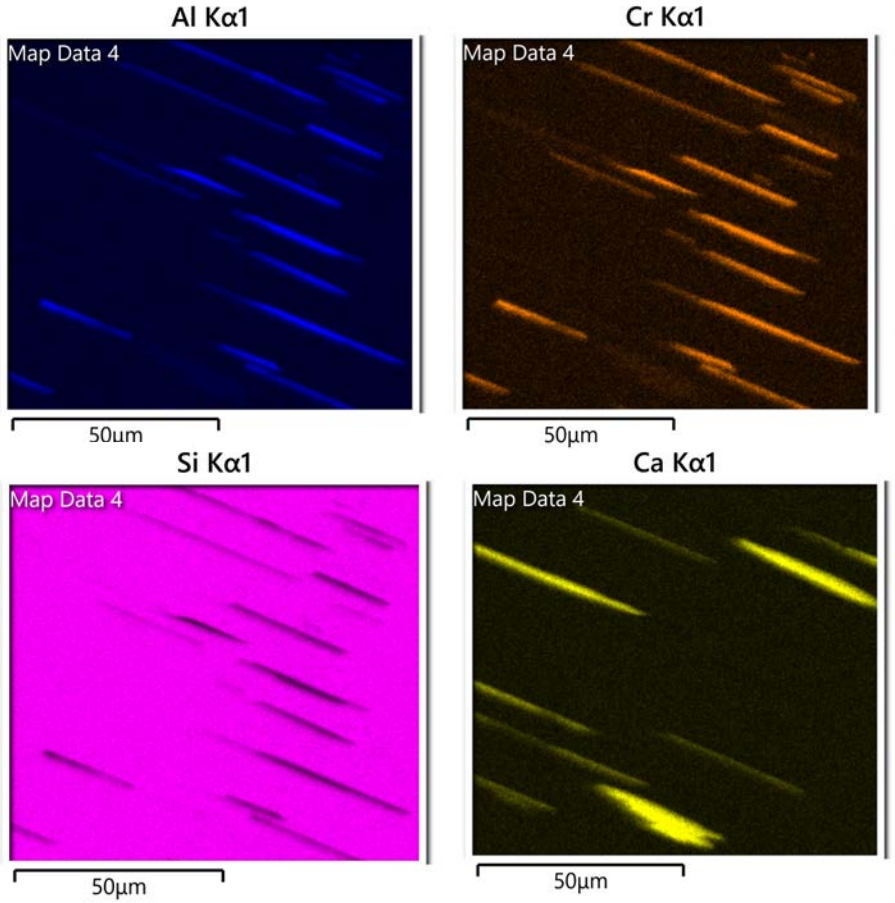

Figure S4d: PAL12: Site 9, Olivine with Cr-spinel lamellae
Step size of the EBSD map: 0.4 µm

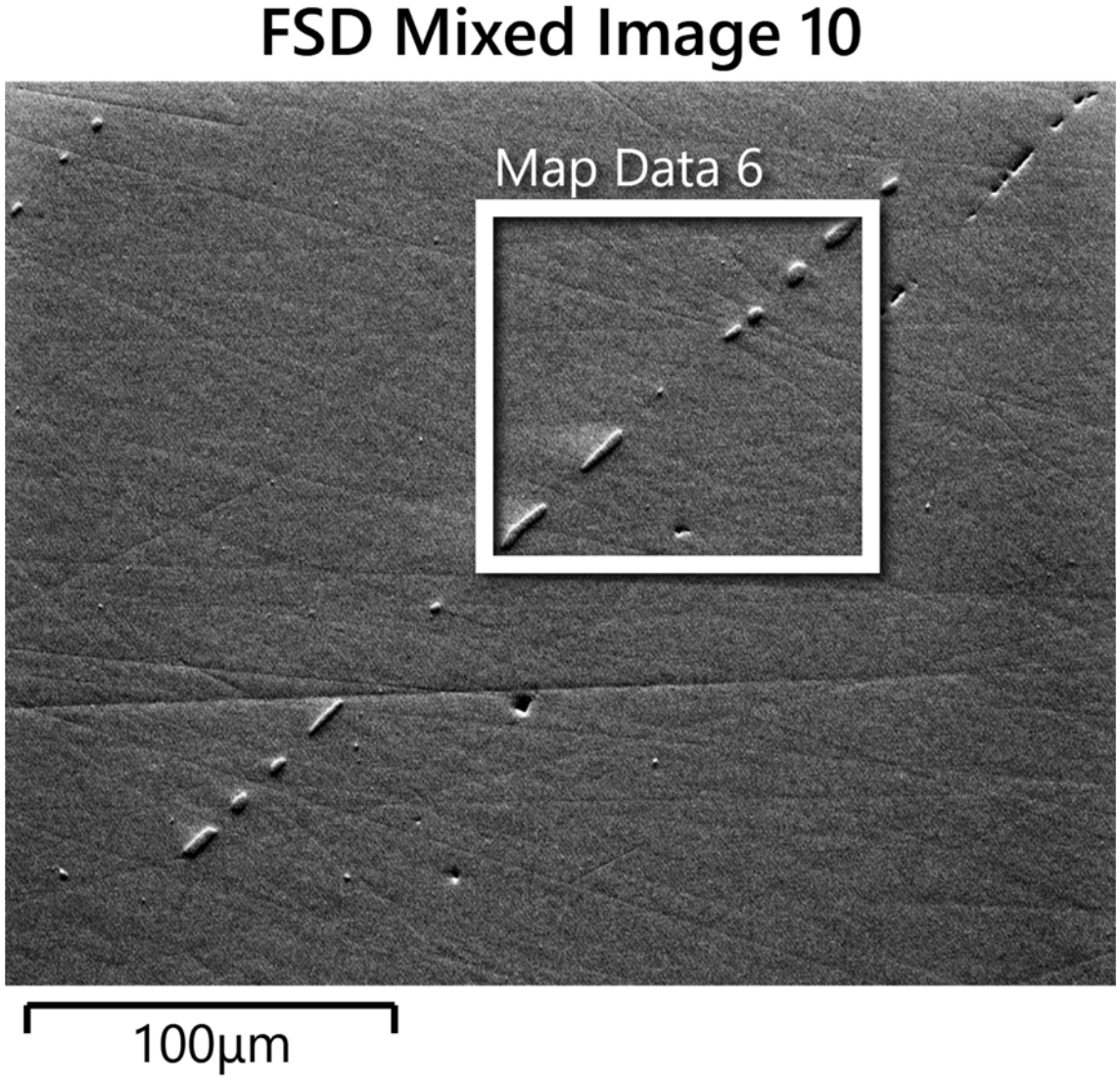

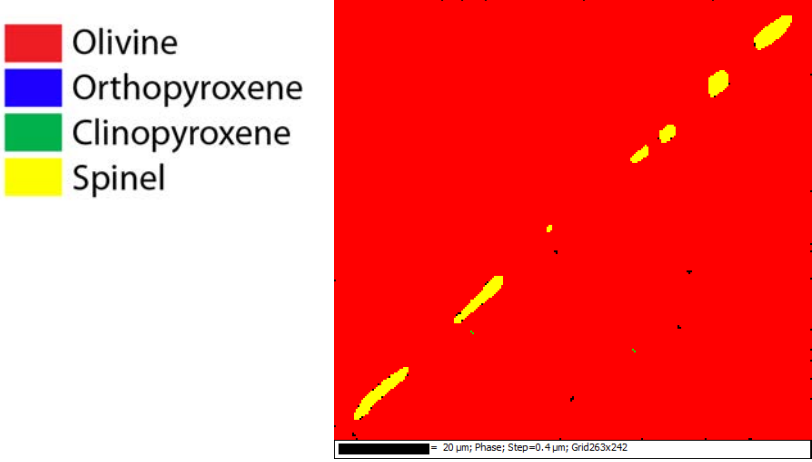

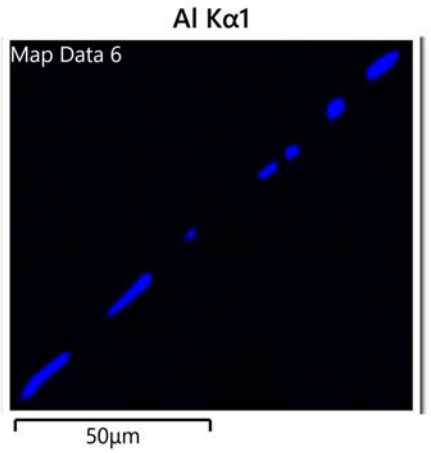

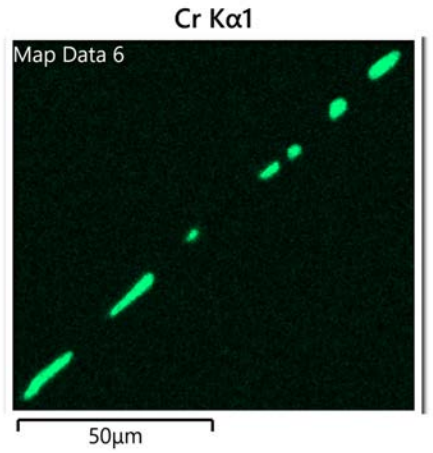

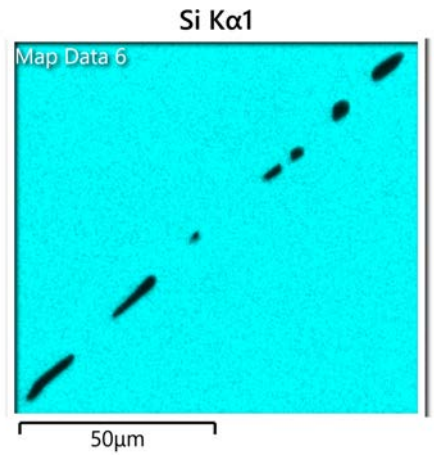

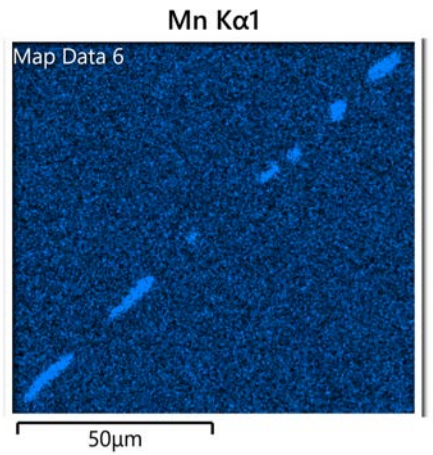

Figure S4e: PAL7: Site 4. Clinopyroxene with Cr-spinel and orthopyroxene lamellae
Step size of the EBSD map: 0.3 µm

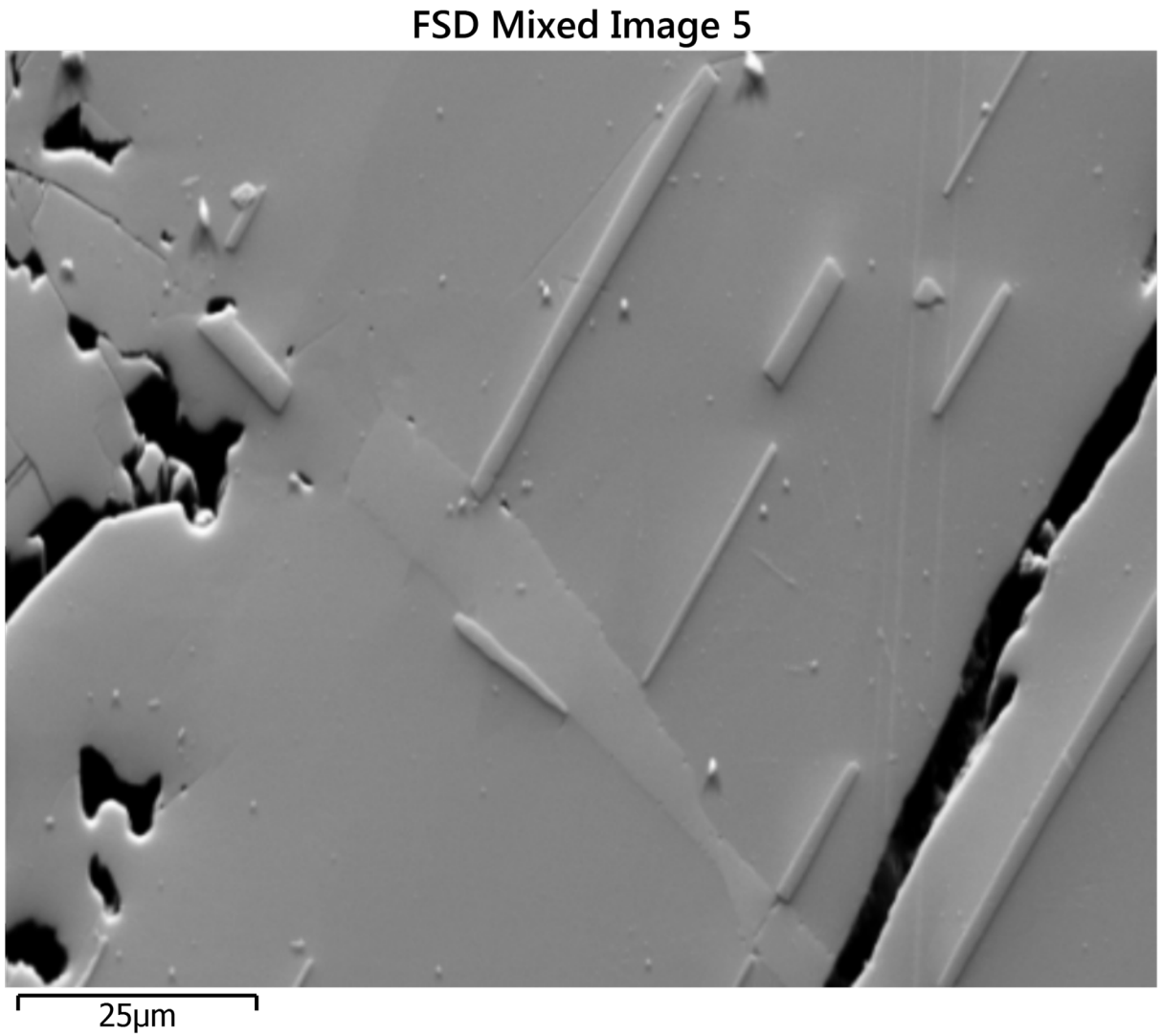

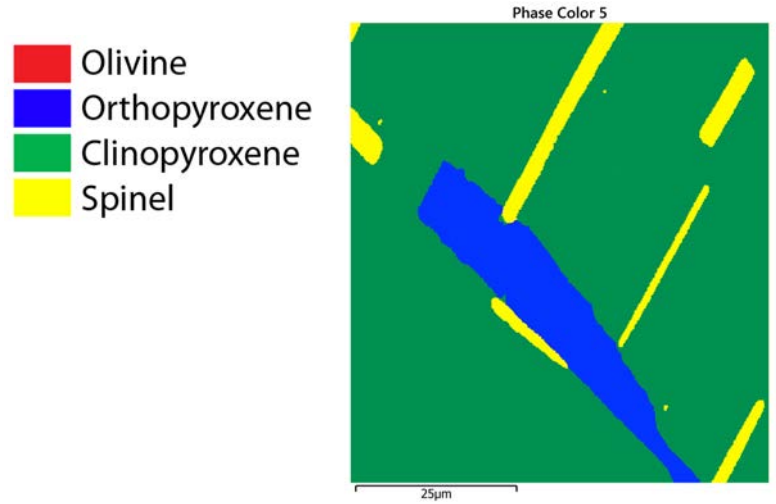

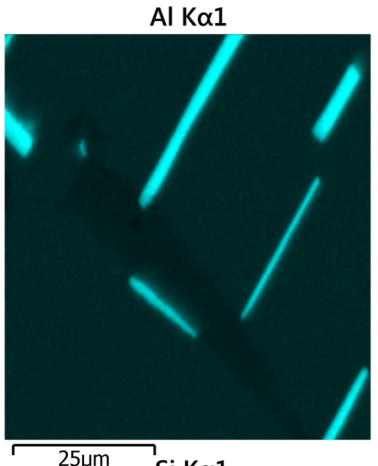

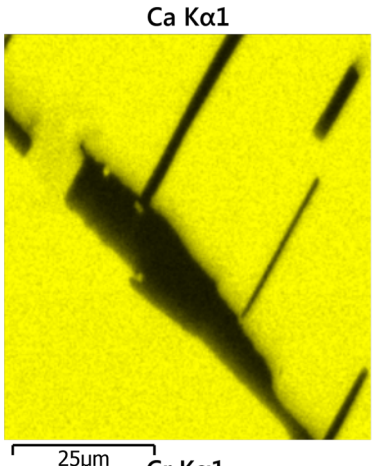

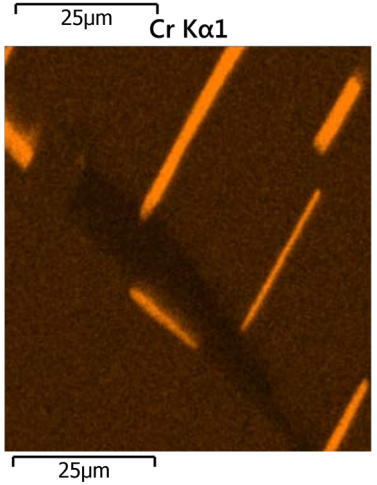

Figure S5: Pole figures illustrating the crystallographic relations between host and exsolved lamellae into orthopyroxene olivine and clinopyroxene.